# JFM PAPERS

# Turbulence statistics and structures in fully developed open channel flows with periodic surface coverages

**Xiaodong Liu**[1] **and Adrian Wing-Keung Law**[1,2],†

[1]School of Civil and Environmental Engineering, Nanyang Technological University, Singapore 639798

[2]Department of Civil and Environmental Engineering, National University of Singapore, Singapore 119077

Modular floating solar farms exhibit periodic open surface coverages due to the strip configuration of floating modules that support the photovoltaic (PV) panels on top. The associated modulations in the surface boundary layer and its turbulence characteristics are investigated in the present study under fully developed open channel flows. Different coverage percentages of 100 % (i.e. full cover), 60 %, 30 % and 0 % (i.e. open surface) were tested and measurements were obtained using particle image velocimetry. The results showed that the turbulence statistics are similar when the coverage decreases from 100 % to 60 %. However, with 30 %, both the turbulence intensities and Reynolds stresses increase substantially, reaching up to 50 % higher compared with the 100 % coverage, and the boundary layer thickness increases by more than 25 %. The local skin friction beneath the openings increases by 50 %. Analysis of spanwise vortices and premultiplied spectra indicates that the periodic coverage elongates the hairpin vortex packets and reduces their inclination angle, imposing limitations on sustainable coherent structures. At 30 %, flow detachment and smaller-scale vortices become dominant, reducing the mean velocities and increasing the turbulence intensities. Decreasing coverage percentage with flow detachment also shifts the energy transfer to higher wavenumbers, increasing energy dissipation and decreasing the bulk flow velocity. The kinetic energy and Reynolds stress carried by very large-scale motions decreases from 40 %–50 % with the 100 % and 60 % coverage to around 30 %–40 % with the 30 % coverage. Further research studies involving spanwise heterogeneity, higher Reynolds number and varying submergence of PV modules are needed for environmental considerations.

**Key words:** turbulent boundary layers

† Email address for correspondence: cewklaw@nus.edu.sg

## 1. Introduction

The surface roughness surrounding wall-bounded flows can induce significant modulations in the turbulence statistics within the flow domain. In canonical channel flows with a height $h_d = 2\delta$ ($\delta$, boundary layer thickness) and characterized by symmetrical top and bottom smooth boundaries, the turbulence characteristics within a fully developed region were found to be statistically stationary (Millikan 1938; Kim, Moin & Moser 1987; Moser, Kim & Mansour 1999). Experimental studies (Wei & Willmarth 1989; Antonia *et al.* 1992) confirmed the expected statistical symmetry about the midplane ($z = \delta$). Within the viscous sublayer ($z^+ < 5$, where $z^+$ is the inner-scaled distance to the wall boundary), the velocity profile followed a linear relation $u^+ = z^+$ ($u^+$ is the normalized velocity by friction velocity). Farther away from the boundary, as $z^+$ exceeds 30, the viscosity's influence diminished, and the velocity profile followed a logarithmic law (Wei & Willmarth 1989), until deviations were observed in the core region ($z/\delta > 0.3$). The buffer layer, between the viscous sublayer and the log-law region, marked the transition from viscosity-dominated to turbulence-dominated flow. Regarding Reynold stresses and related turbulence statistics, the log-law region exhibited approximate self-similarity, with production and dissipation nearly balancing each other and minimal transport of kinetic energy.

Zero-pressure-gradient boundary layer (ZPGBL) and open channel flows also exhibit distinct turbulence characteristics influenced by the surface boundary conditions. In ZPGBLs with a turbulent–non-turbulent boundary (Klebanoff 1955; Spalart 1988; Marusic, Uddin & Perry 1997), the behaviour in the viscous sublayer was observed to closely mirror that of channel flows, while in the buffer layer, the van Driest damping function was observed (Van Driest 1956). Coles (1956) also demonstrated that the mean velocity profile in the defect layer ($z/\delta > 0.2$) can be well represented by the sum of the law of wall and wake function, while the profiles of Reynold stresses and related turbulence statistics diminished smoothly to zero near the boundary. In open channel flows with an atmospheric surface boundary (Steffler, Rajaratnam & Peterson 1985; Nezu & Rodi 1986; Cardoso, Graf & Gust 1989), the viscous sublayer and buffer layer exhibited similar characteristics with ZPGBL, while the air–fluid surface reduced the wake length in the outer layer comparatively. The damping effect of the atmospheric surface boundary in open channel flows also caused the redistribution of the turbulent kinetic energy (TKE) close to the free surface, i.e. the reduction of the wall-normal velocity fluctuations and the increase of streamwise and spanwise components.

The presence of a solid cover on the open water surface imposes a change in the surface boundary conditions which modulates the turbulence statistics within the flow domain, particularly interacting with the turbulence generated by the bed roughness at the bottom of the flow domain. Muste, Braileanu & Ettema (2000) and Robert & Tran (2012) conducted experimental measurements of turbulence characteristics in ice-covered channels. They found that the presence of the ice cover increased the flow depth and TKE compared with open water flows due to the non-slip boundary, resulting in more negative Reynolds stresses near the covers. Zhang *et al.* (2021) proposed analytical models for the longitudinal velocity, Reynolds stress and turbulence intensity in fully and partially ice-covered channels, and verified with experimental measurements. Wang *et al.* (2020, 2021) developed analytical models to predict the streamwise velocity distribution in compound channels with ice covers, considering factors such as channel bed friction, ice cover resistance and secondary currents, with applications to full cover and symmetrical shore cover conditions.

The turbulence statistics with different surface boundaries is related to the changes in the turbulent structures instigated by the boundaries. For example, wall turbulence is inherently non-isotropic and many studies investigated the organized motions with their spatial coherence near the wall (Robinson 1991; Marusic & Monty 2019). Recent research shifted the focus from the viscous-dominated near-wall region where local TKE production peaked, to the inertial-dominated logarithmic region which was pivotal for bulk TKE production at high Reynolds numbers. In the near-wall region, coherent structures were often associated with low-speed streaks, which were elongated regions of reduced streamwise velocity that extend across the boundary layer (Kline *et al.* 1967; Smith & Metzler 1983; Gad-el Hak & Bandyopadhyay 1994). A related phenomenon was the bursting process, which involved the periodic ejection of low-speed fluid from the near-wall region into the outer layer, followed by the sweep of high-speed fluid towards the wall. These events were closely related to the motion of hairpin vortices, which were leg-like structures that extended from the wall into the flow and were instrumental in the transfer of momentum from the buffer layer to the log layer (Head & Bandyopadhyay 1981; Marušić & Perry 1995; Adrian, Meinhart & Tomkins 2000). In the log-law region, coherent structures were typically characterized by the presence of streamwise-oriented vortices and packets of hairpin vortices that spanned a significant portion of the boundary layer. These structures were often referred to as very large-scale motions (VLSMs), and their wavelengths can be an order of magnitude larger than the boundary layer thickness (Kovasznay, Kibens & Blackwelder 1970; Kim & Adrian 1999). The VLSMs can contribute significantly to the streamwise turbulence intensity, Reynolds shear stress and the resulting net force exerted on the mean flow. They were posited to arise from the coherent alignment of large-scale motions, such as turbulent bulges or packets of hairpin vortices, induced by the collective behaviour of near-wall structures. This alignment, in turn, enhanced the generation of the latter structures, termed a cosupporting cycle by Toh & Itano (2005) or a closed-loop feedback cycle by Adrian & Marusic (2012). Particularly within the inner region of the log layer, there was an abundance of prograde spanwise vortices aligning with the characteristic traits of hairpin vortex heads, which served as fundamental constituents of larger-scale vortex organization in the outer flow regime (Adrian *et al.* 2000; Wu & Christensen 2006; Zhong *et al.* 2015). Moreover, VLSMs were instrumental in the conveyance of a notable fraction of kinetic energy (40 %–65 %) and Reynolds shear stress (30 %–50 %) across diverse flow configurations (Guala, Hommema & Adrian 2006; Balakumar & Adrian 2007; Duan *et al.* 2020*a*).

Due to the global interest of renewable energy production, the installation of floating photovoltaic (PV) systems have been growing rapidly in recent years (Ghosh 2023; Huang *et al.* 2023; Shi *et al.* 2023). Large-scale floating solar farms typically consist of interconnected buoyant pontoon modules that can number in the millions, supporting PV panels for solar power conversion (Dai *et al.* 2020; Sree *et al.* 2022; Bi & Law 2023). As a result, the interplay of millions of interconnected modules and the presence of periodic cavities within the floating solar farm engender a novel open-surface boundary with periodic coverages, and its effect on the turbulence characteristics of the water column underneath needs to be comprehensively understood for environmental considerations. However, there has not been any study reported in the literature as far as we are aware. In the marine environment, a typical floating PV module can convert a substantial portion of the incoming solar radiation into heat. Despite the cooling effect of ambient water, the average temperature of a single floating PV module can rise from 25 °C to 48.8 °C under constant solar radiation intensity of 417 W m$^{-2}$ within 60 min (Azmi *et al.* 2013). The heterogeneous distribution of temperature in both streamwise (Stoll & Porté-Agel

2009) and spanwise (Bon & Meyers 2022; Salesky, Calaf & Anderson 2022) directions can significantly affect the flow properties in channel flows due to stratification. This aspect is not included in the present study, which primarily focuses on the heterogeneity of surface roughness and its effects on turbulent flow characteristics.

In the context of engineering and atmospheric flows, a vast body of literature had examined the effects of varying roughness on solid surfaces, including transitions from rough-to-smooth and smooth-to-rough surfaces, and the related internal boundary layers (Bou-Zeid *et al.* 2020; Kadivar, Tormey & McGranaghan 2021). The consensus from most studies is that the outer-layer similarity with smooth-wall boundary layers holds for a large range of three-dimensional roughness types and sizes when the ratio of the roughness height $k$ to $\delta$ is less than 1/10 (Castro 2007). However, two-dimensional (2-D) k-type roughness may exhibit different behaviour. Keirsbulck *et al.* (2002) reported boundary layer experiments with 2-D transverse bars and $p/k = 3.33$ (where $p$ is the streamwise rod spacing) and they found reasonable similarity with smooth-wall flows for the Reynolds stresses in the outer flow, while Djenidi *et al.* (2008) conducted experiments with 2-D transverse square bars with $p/k$ ranging from 8 to 16 and they observed differences in the turbulence structure, including larger Reynolds stresses in the outer layer compared with smooth-wall cases. Lee, Sung & Krogstad (2011) also reported an increase of both the Reynolds normal stresses and the Reynolds shear stress across most of the boundary layer. Comparatively, in canonical channel flows, 2-D roughness does not seem to produce the differences observed in the boundary layers. Krogstad *et al.* (2005) conducted experiments and direct numerical simulations (DNS) for symmetric channel flows with 2-D k-type transverse square bars and $p/k = 8$ on both bounding walls. They also found no significant differences from the smooth-wall case in the outer flows.

This study investigated experimentally the above novel open-surface boundary interspersed with periodic coverages in fully developed open channel flows. Particle image velocimetry (PIV) measurements were conducted in the streamwise–wall-normal plane. Turbulent statistics were initially derived from these measurements and compared with established channel and open-channel flows including conventional 2-D roughness. Subsequently, a vortex identification method was developed to isolate resolved vortices from the background turbulence to facilitate in-depth population studies of near-boundary turbulent structures. Furthermore, the premultiplied power spectrum was employed to analyse the contribution to turbulence from varying wavenumbers. Finally, the portion of TKE and Reynolds shear stress carried by VLSMs was discussed.

## 2. Experiments

Experiments were conducted in a recirculating flume as shown in figure 1(*a*) in the Hydraulic Modelling Laboratory at Nanyang Technological University. The flume had dimensions of 11 m (length), 0.6 m (width) and 0.7 m (depth). Its transparent side and bottom walls facilitated optical observations via the PIV technique. The channel slope $S$ was constant at 0.0005 throughout all tests. Honeycombs were strategically positioned to homogenize the flow at the flume entrance. Flow rates were kept constant and monitored using an electromagnetic flowmeter. The measurement section, positioned at 9.5 m downstream of the flume entrance, ensured fully developed flow conditions. This distance, approximately 190 times the hydraulic depth $h_d$, exceeded the criteria for fully developed open channel flows as suggested by Kirgköz & Ardiçlioğlu (1997) and Lien *et al.* (2004), with values of $76h_d$ and $150h_d$, respectively. Additionally, to safely ensure
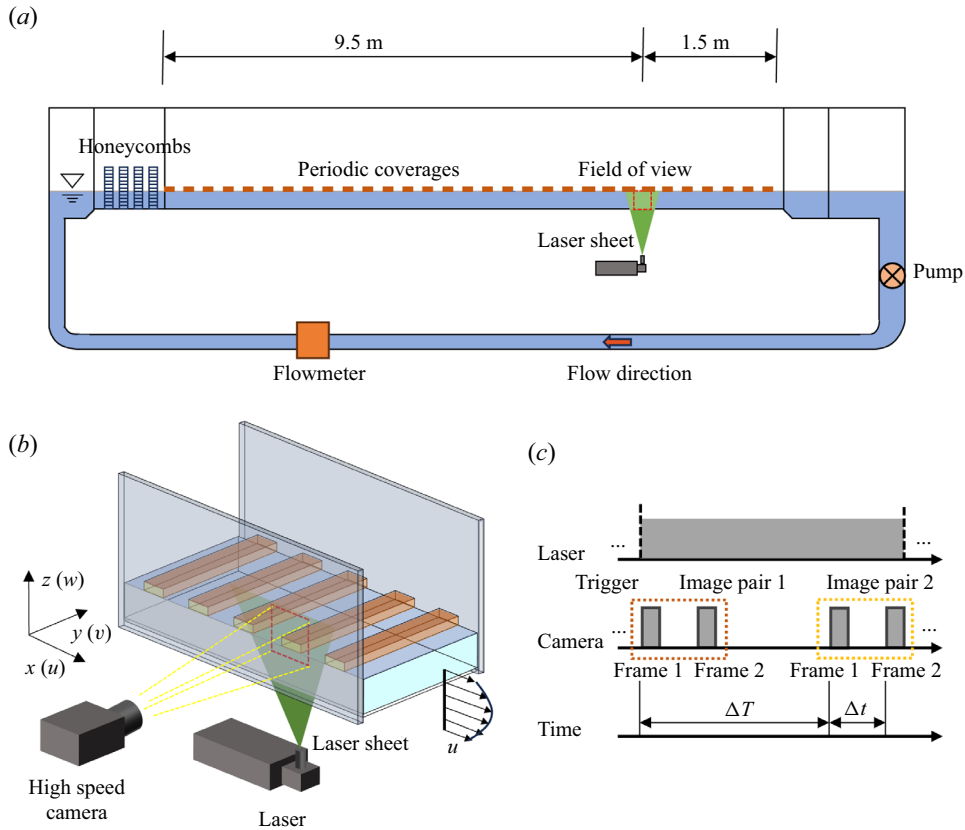
Figure 1. (*a*) Schematic diagram of the flume with the width of 60 cm. (*b*) The set-up of semiopen channel flow and the PIV system and (*c*) operation mode.

that the flow conditions were fully developed, detailed measurements were also taken at 8 m downstream of the flume entrance for checking.

The PIV measurements were performed in a streamwise wall-normal plane in the channel as shown in figure 1(*b*). A laser sheet, 1.5 mm thick, was generated from a 5 W air-cooled laser with a wavelength of 532 nm, and it served as the light source to illuminate the field of view. A high-speed CMOS (complementary metal–oxide–semiconductor) camera (Phantom Miro 120 with a Sigma 105 mm f/2.8 prime lens) was employed to capture the images. Polyamide seeding particles (Dantec Dynamics, PSP-50) with an average diameter of $50\,\mu\text{m}$ acted as tracer particles. The PIV mode in the camera control software (Phantom Camera Control v3.8) was utilized for high-frequency sampling, as shown in figure 1(*c*). With constant illumination by the continuous laser, the exposure time for each frame was set as $300\,\mu\text{s}$ to ascertain the capture of images containing an adequate number of particles. The time interval between the two frames within each image pair, $\Delta t$, was fixed to $500\,\mu\text{s}$, satisfying the one-quarter rule (Adrian & Westerweel 2011). The sampling rate, $F_s$, was set to 100 Hz, yielding a corresponding inner-scaled time interval between successive velocity fields, $\Delta T^+$, in the range of 1.4–1.8, satisfying the criterion proposed by Duan *et al.* (2020*b*) for resolving small-scale energetic motions. The total image acquisition time $T_{total}$, during which a total of 359 064 images were taken and the streamwise distance of the mean flow movement $U_m T_{total}$ exceeded $10\,000 h_d$, which

ensured the convergence of spectral results at the largest energetic wavelength (Duan *et al.* 2020*a*).

The experimental conditions with varying coverage percentages are detailed in table 1. The configuration of periodic coverages for floating solar farms typically ranges from tubular modules made of high-density polyethylene pipes along with steel or aluminium, leading to small coverage, to full high-density polyethylene rafts of smaller dimensions with moderate coverage, and gable slender floating pontoon structures with large coverage (Ghosh 2023). To investigate these variations, we considered scenarios with low (30 %) and large (60 %) coverage, alongside open surface (0 %) and full cover (100 %), as shown in figure 2. The geometry of the PV module was based on the floating solar PV cell test-bed launched in Singapore (Dai *et al.* 2020). This set-up induces both streamwise and spanwise heterogeneous surface roughness due to the three-dimensional meshing geometry. In the present study, only the module geometry in the streamwise direction was examined. The PV module was made with a scale of $1:60$ ($\lambda$) based on the Froude similarity, resulting in a 5 cm length (the summation of a coverage and air strip) and 3 mm thickness. The submergence was typically kept small and less than 1 mm due to moisture, which was also considered as the roughness height $k$. These modules were interconnected using 2-cm-wide strips positioned near both sidewalls, ensuring a practical and straightforward set-up. While large-scale floating solar farms are typically designed for water depths greater than the PV module length (Dai *et al.* 2020; Huang *et al.* 2023), this study utilized a water depth comparable to the PV module length ($h_d$) due to experimental constraints. Nevertheless, $\delta/k \approx 25$ was sufficiently large for the boundary layer thickness of the covered surface and channel bottom in the experiments. Thus, the water depth in the experiments was able to accommodate the two boundaries sufficiently to minimise their interactions.

The PIV measurement parameters for all the four coverage cases are summarized in table 2. In each case, the acquired particle images underwent postprocessing using the PIVlab, an open-source GUI-based PIV software, the accuracy of which has been validated in the literature (Thielicke & Sonntag 2021). The size of field of view was $640 \times 480$ pixels and the corresponding resolution was 8.33 pixel mm$^{-1}$. The initial interrogation window size was set at $64 \times 64$ pixels. Following three passes with a 50 % overlap, the final window size, containing 2–4 particles, was reduced to $16 \times 16$ pixels.

## 3. Methodology

The notations $x$, $y$ and $z$ denote the streamwise, spanwise and wall-normal directions, respectively, as shown in figure 1. The instantaneous velocities along these directions are denoted as $u$, $v$ and $w$, respectively, which can be decomposed through Reynolds decomposition into the mean part, represented by $U$, $V$ and $W$, and the fluctuation part, denoted as $u'$, $v'$ and $w'$. The surface boundary layer thickness $\delta_s$ and the surface momentum boundary layer thickness $\theta_s$ are defined with respect to the boundary layer attached to the periodic coverage, and $\delta_b$ is corresponding to the bottom. Reynolds numbers can be calculated accordingly. Friction velocities associated with the coverage, represented as $u_\tau^s$, and the bottom, denoted as $u_\tau^b$, are defined, respectively. All quantities normalized with friction velocity corresponding to their boundary layer and kinematic viscosity are represented with a superscript +, and a top bar − denotes the ensemble average. All the above variables are summarized in table 1.

| Test | Coverage percentage (%) | $h_d$ (×10⁻² m) | $U_m$ (m s⁻¹) | $u_\tau^b$ (m s⁻¹) | $u_\tau^s$ (m s⁻¹) | $\delta_s$ (×10⁻² m) | $\delta_b$ (×10⁻² m) | $\theta_s$ (×10⁻² m) | $Fr_{\delta_s}$ | $Re_{\delta_s}$ | $Re_{\tau_s}$ |
|---|---|---|---|---|---|---|---|---|---|---|---|
| T1 | 100 | 5.0 | 0.211 | 0.0130 | 0.0125 | 2.64 | 2.36 | 0.24 | 0.43 | 6259 | 373 |
| T2 | 60 | 5.0 | 0.198 | 0.0129 | 0.0126 | 2.63 | 2.37 | 0.22 | 0.40 | 5821 | 372 |
| T3 | 30 | 5.0 | 0.197 | 0.0129 | 0.0126 | 3.22 | 1.78 | 0.34 | 0.40 | 7127 | 455 |
| T4 | 0 | 5.0 | 0.217 | 0.0121 | — | — | 5.00 | — | — | — | — |

Table 1. Test conditions: $h_d$, water depth; $U_m$, depth mean velocity; $u_\tau^b$, bottom friction velocity, determined based on the log-law using the lower part of the water depth; $u_\tau^s$, surface friction velocity; $\delta_s$, surface boundary layer thickness generated by the coverage; $\delta_b$, bottom boundary layer thickness generated by the bottom; $\theta_s$, momentum boundary layer thickness corresponding to $\delta_s$; $Fr_{\delta_s} = U_m/\sqrt{g\delta_s}$, Froude number; $Re_{\delta_s} = U_m\delta_s/\nu$, Reynolds number ($\nu = 8.9 \times 10^{-3}$ cm² s⁻¹); $Re_{\tau_s} = u_\tau^s\delta_s/\nu$, friction Reynolds number.
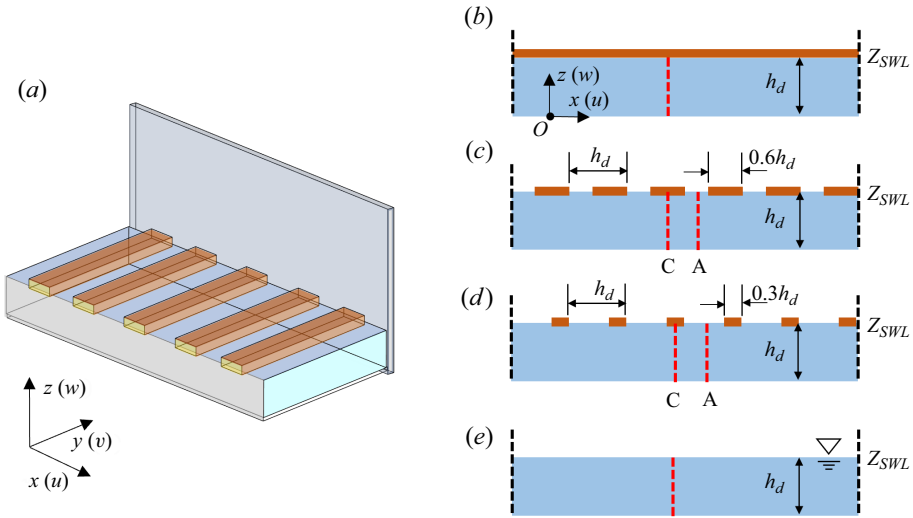
Figure 2. (*a*) Perspective view with periodic coverages and side view with coverage of (*b*) 100 %, (*c*) 60 %, (*d*) 30 % and (*e*) 0 %.

| Test | Image size (pixels) | Resolution (pixel mm$^{-1}$) | $F_s$ (Hz) | $\Delta T^+$ | $\Delta T U_m/\delta_s$ | Number of flow fields | $U_m T_{total}/\delta_s$ | $\Delta y^+ (\Delta x^+)$ |
|------|------|------|------|------|------|------|------|------|
| T1 | 640 × 480 | 8.33 | 100 | 1.8 | 0.08 | 359 064 | 28 693 | 13.4 |
| T2 | 640 × 480 | 8.33 | 100 | 1.5 | 0.08 | 359 064 | 20 727 | 13.6 |
| T3 | 640 × 480 | 8.33 | 100 | 1.4 | 0.06 | 359 064 | 22 075 | 13.6 |
| T4 | 640 × 480 | 8.33 | 100 | — | — | 359 064 | — | — |

Table 2. The PIV parameters: $F_s$, the sampling frequency of the velocity fields; $\Delta T^+ = \Delta T/(\nu/u_\tau^{s\,2})$ and $\Delta T U_m/\delta_s$, inner- and outer-scaled time interval between successive velocity fields; $T_{total}$, total image acquisition time; $\Delta y^+ = \Delta y/(\nu/u_\tau^s)$ $(\Delta x^+)$, the inner-scaled vector spacing in the wall-normal (or streamwise) direction.

For both smooth-wall and rough-wall, the mean streamwise velocity distribution in the log-law region is described by

$$U^+ = \frac{1}{\kappa} \ln \Delta z^+ + A - \Delta U^+, \tag{3.1}$$

where $\Delta z^+ = (\Delta z + \varepsilon)u_\tau/\nu$ (Krogstadt & Antonia 1999; Keirsbulck *et al.* 2002). Here $\varepsilon$ is the origin shift for the rough-wall (zero for smooth wall) and $\Delta z$ is the distance measured from the top of the roughness. The constants $\kappa$ and $A$ are empirically determined to be 0.41 and 5, respectively. Here $\Delta U^+ = (U_r - U_s)/u_\tau$ is the roughness function (zero for smooth-wall). In the present study, both $u_\tau^s$ and $u_\tau^b$ were determined by fitting the above equation, which accounts for the geometrical similarity between the periodic coverages and 2-D k-type roughness. The difference due to the periodic air strips is discussed in the following sections.

**1000** A6-8

The local skin friction (Fukagata, Iwamoto & Kasagi 2002; Stroh *et al.* 2020) can be calculated by

$$C_f = \frac{6\nu}{U_m \delta} + 6 \int_0^1 \left(1 - \frac{z}{\delta}\right) \frac{-\overline{u'w'}}{U_m^2} \, \mathrm{d}z, \tag{3.2}$$

where the skin friction coefficient is decomposed into the laminar component $C_f^{lam}$ (the first term on the right-hand side) and the turbulent component $C_f^{tur}$ (the second term on the right-hand side).

For momentum transport under varying coverage conditions, the decomposed momentum balance of the total shear stress is expressed as (Stroh *et al.* 2020)

$$\tau = \nu \frac{\mathrm{d}U}{\mathrm{d}z} - \overline{u'w'}, \tag{3.3}$$

where the first term on the right-hand side represents the viscous shear stress, and the second term represents the turbulent shear stress.

### 3.1. *Vortex identification*

The PIV measurements (Adrian *et al.* 2000; Wu & Christensen 2006; Zhong *et al.* 2015) in a turbulent boundary layer with friction Reynolds numbers $Re_\tau$ up to $O(4)$ illustrated the presence of prograde spanwise vortex structures aligning in the streamwise direction to form larger-scale vortex packets, consistent with the characteristic features of hairpin vortices. The findings underscored the interplay between the near-wall ejections and progression of large-scale motions. In the previous literature, prograde spanwise vortex structures were typically referred to as clockwise vortices, denoting vortex cores rotating from the upstream to the downstream side, while retrograde structures exhibited the opposite. Prograde vortices induced a region of low-momentum fluid situated below and upstream of the vortex head, with this region inclined approximately in the streamwise direction and becoming more parallel to the wall as the proximity to the wall increased (Adrian *et al.* 2000). This observation provided evidence for the hairpin vortex and the associated momentum transport. Although our present study focuses on the surface boundary, we retain the terms prograde and retrograde vortex to represent their physical mechanisms, despite the rotational directions being opposite to those respective in the literature.

Several effective methods have been proposed to extract spanwise vortices from background turbulence (Chakraborty, Balachandar & Adrian 2005). Among them, the $\lambda_{ci}$ criterion by Zhou *et al.* (1999), also known as swirling strength, is widely used, primarily because the vortex identification via swirling strength remains Galilean invariant and does not erroneously include regions of intense shear lacking rotation. To determine the direction of rotation, Tomkins & Adrian (2003) introduced the modified criterion as follows:

$$\Lambda_{ci}(x, z) = \lambda_{ci} \frac{\omega_y(x, z)}{|\omega_y(x, z)|}, \tag{3.4}$$

where $\omega_y$ is the instantaneous fluctuating spanwise vorticity.

Given that $\Lambda_{ci}$ is highly intermittent, being non-zero only within vortex cores, its mean value is significantly smaller than its root mean square $\Lambda_{ci}^{rms}$. Wu & Christensen (2006)

proposed a normalized swirling strength represented as

$$\tilde{\Lambda}_{ci}(x, z) = \frac{\Lambda_{ci}(x, z)}{\Lambda_{ci}^{rms}(z)}. \tag{3.5}$$

A threshold of $\tilde{\Lambda}_{ci}(x, z) = 1.5$ is recommended by Wu & Christensen (2006) to delineate the boundaries of the vortex sections. In terms of orientation of vortices beneath the periodic coverage in the present study, a negative value of $\Lambda_{ci}$ would denote a prograde vortex, whereas a positive value would indicate a retrograde vortex. Besides selecting an appropriate swirling-strength threshold, the resolution of the PIV measurements also inherently limits the size of the smallest resolvable vortex. Consequently, clusters of $\tilde{\Lambda}_{ci}$ with fewer than three grid points across their span in both $x$ and $z$ directions, having $\tilde{\Lambda}_{ci}(x, z) = 1.5$, are disregarded due to insufficient spatial resolutions.

Upon isolating the individual vortices, their population density $\Pi_{p(r)}(z)$ can be quantified as the ensemble-averaged number of prograde (retrograde) spanwise vortices, $N_{p(r)}$, residing in rectangular areas of wall-normal height $3\Delta z/\delta$ and streamwise width $L_x/\delta$, centred at $z$, as defined by Wu & Christensen (2006)

$$\Pi_{p(r)}(z/\delta) = \frac{N_{p(r)}(z/\delta)}{\dfrac{3\Delta z}{\delta}\dfrac{L_x}{\delta}}. \tag{3.6}$$

### 3.2. *Premultiplied spectra*

For simplicity, we denote the streamwise and wall-normal fluctuating velocity signals as $u_i'$ ($i = 1, 2$) with $u_1' = u'$ and $u_2' = w'$. The corresponding power spectrum can be defined as

$$\Phi_{u_i'u_j'} = c|F_{u_i'}(f)F_{u_j'}^*(f)|, \tag{3.7}$$

where $F_{u_i'}(f)$ represents the Fourier transform of the fluctuating velocity signal $u_i'$, $f$ is the frequency, the superscript $*$ denotes the complex conjugate, $|\ |$ indicates the modulus and $c$ is a constant determined by satisfying the following equation:

$$\overline{u_i'u_j'} = \int_0^\infty \Phi_{u_i'u_j'}(f)\,\mathrm{d}f. \tag{3.8}$$

According to Taylor's frozen turbulence hypothesis (Taylor 1938), the frequency-based spectrum $\Phi_{u_i'u_j'}(f)$ converted to a streamwise wavenumber $k_x$ (or wavelength $\Lambda$) spectrum $\Phi_{u_i'u_j'}(k_x)$ (or $\Phi_{u_i'u_j'}(\Lambda)$) using the relationships

$$\left.\begin{aligned} k_x &= \frac{2\pi f}{U(z)}, \\ \Lambda &= \frac{2\pi}{k_x}, \end{aligned}\right\} \tag{3.9}$$

where $U(z)$ represents the mean streamwise velocity at $z$.

Utilizing premultiplied spectral analysis with the plot of $k_x\Phi_{u_i'u_j'}(k_x)$ versus $k_x$ (or $\Lambda$), enables a clear depiction of the contributions of different wavelengths to the overall spectrum, facilitating the identification of wavelengths with peak spectral densities. Furthermore, the relative contributions of distinct wavelengths to the total energy (or shear
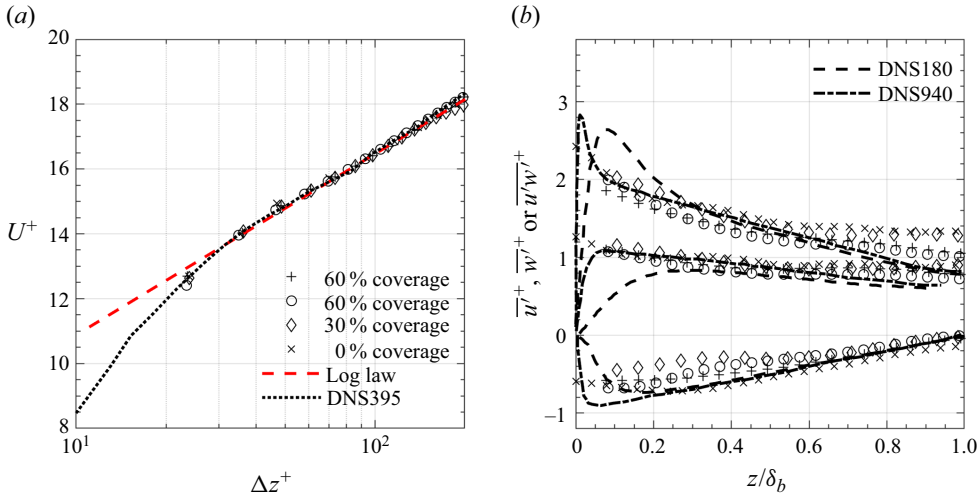
Figure 3. Wall-normal profiles of turbulence statistical parameters: (*a*) mean velocity; (*b*) turbulence intensity and Reynolds shear stress. The DNS results of closed channel flows at $Re_\tau = 180$ (DNS180) and 395 (DNS395) are from Moser *et al.* (1999). The DNS results of closed channel at $Re_\tau = 940$ (DNS940) are from Hoyas & Jiménez (2008).

stress) can be identified through the analysis. The cumulative contributions $\gamma_{u_i' u_j'}$ from all wavenumbers between $k_x = 2\pi/\Lambda$ and infinity can be computed as follows:

$$\gamma_{u_i' u_j'}\left(k_x = \frac{2\pi}{\Lambda}\right) = 1 - \frac{\int_0^{k_x} \Phi_{u_i' u_j'}(k_x) \, \mathrm{d}k_x}{\int_0^\infty \Phi_{u_i' u_j'}(k_x) \, \mathrm{d}k_x}. \tag{3.10}$$

## 4. Validation

As discussed earlier, wall turbulence with a smooth boundary had been extensively documented, encompassing turbulent statistics across a broad range of Reynolds numbers *Re* up to $O(6)$ (Pope 2001). Similarities were observed in the near-wall region (Monty *et al.* 2009), despite the variations introduced by diverse surface boundaries on top. In the present study, the flow proximal to the bottom wall is primarily influenced by the wall boundary, thereby facilitating comparisons with prior studies to ascertain the accuracy of experimental data.

Non-dimensional profiles of the mean velocity, turbulence intensity ($\overline{u'}^+ = \sqrt{\overline{u'^2}}/u_\tau^b$ and $\overline{w'}^+ = \sqrt{\overline{w'^2}}/u_\tau^b$) and Reynolds shear stress ($\overline{u'w'}^+ = \overline{u'w'}/u_\tau^{b\,2}$) are shown in figure 3 within the bottom boundary layer ($z < \delta_b$) for all four cases. The mean velocity profiles closely adhere to the DNS results of closed channel flow (Moser *et al.* 1999) with $Re_\tau = 395$, exhibiting a well-defined logarithmic distribution (Nezu & Rodi 1986). Turbulence intensities are found to be consistent with DNS findings (Moser *et al.* 1999; Hoyas & Jiménez 2008) in the near-wall and log layer regions. For the bottom boundary layer, the obtained experimental data sufficiently support the turbulence statistics analysis under various coverage conditions.

At each wall-normal location, the Welch's overlapped segment averaging method was utilized to derive the velocity signal spectrum. To mitigate spectral leakage arising from truncation at segment edges, a Hamming window, known for its efficacy in
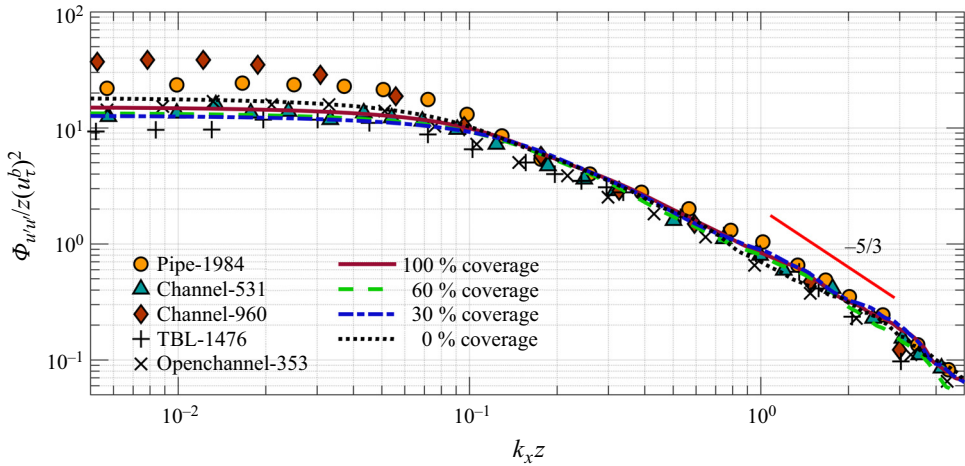
Figure 4. Wavenumber spectrum for streamwise velocity fluctuation at $z/\delta_b = 0.1$. The results of pipe flow (Pipe-1984) are from Kim & Adrian (1999) with $Re_\tau = 1984$ and $z/R = 0.084$ ($R$ is the pipe radius). The results of open-channel flow (Openchannel-353) are from Duan *et al.* (2020*a*) with $Re_\tau = 353$ and $z/h_d = 0.1$. The remaining results are from the closed channel flow and TBL in Balakumar & Adrian (2007): Channel-531 with $Re_\tau = 531$ and $z/h_d = 0.11$; Channel-960 with $Re_\tau = 960$ and $z/h_d = 0.11$; TBL-476 with $Re_\tau = 476$ and $z/\delta = 0.11$.

discrete Fourier transforms on PIV data (de Kat *et al.* 2013), was employed prior to the transformation. In accordance with Duan *et al.* (2020*a*), a nine-point Gaussian kernel was applied to the raw velocity signals to mitigate the contamination from high-frequency measurement noises, stemming from the constrained interrogation window size, and a bandwidth moving filter was implemented to further refine the unfiltered spectrum for the subsequent premultiplied spectral analysis. Figure 4 showcases the filtered spectrum of streamwise velocity fluctuations, juxtaposed with spectral data from other canonical wall-bounded turbulent flows (pipe, closed channel, open channel flow and turbulent boundary layer (TBL)) obtained at equivalent $z$ locations and Reynolds numbers (Kim & Adrian 1999; Balakumar & Adrian 2007; Duan *et al.* 2020*a*) for comparative analysis. A high degree of concordance is evident between the current filtered spectrum and those from other flows, affirming both the precision of the measurements and the soundness of the postprocessing methodology employed.

## 5. Turbulent statistics

### 5.1. *Mean velocity*

The non-dimensional profiles of mean velocity $U/U_m$ against $z/h_d$ at different cross-sections C and A (beneath the cover and air strip, respectively, as shown in figure 2), representing the 60 % and 30 % coverages, respectively, are shown in figure 5, with the 100 % and 0 % coverages included for comparison. In both cases, the velocity beneath the cover strip exhibits a slight decrease compared with the air strip, particularly in the proximity of the coverages. The velocity profiles of the lower bottom part of the 60 % coverage closely resembles that of the 100 % coverage, albeit with some defects noted in the upper coverage region. Conversely, the upper coverage region of the 30 % coverage displays more pronounced defects, leading to an increase in velocity in the lower part for compensation. Consequently, maximum velocities under periodically covered conditions
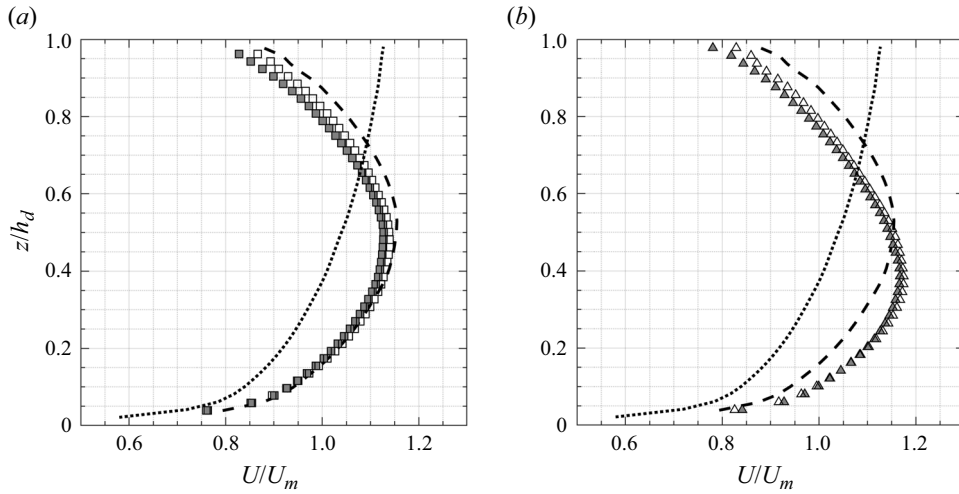
Figure 5. Mean streamwise velocity beneath 100 % coverage (- - - -), cover (■, grey) and air (□) strip of 60 % (shown as cross-sections C and A in figure 2), cover (▲, grey) and air (△) strip of 30 % and 0 % coverage (dotted line).

are observed closer to the bottom as the coverage percentage decreases. This variation affects the definition of the corresponding boundary layer thickness $\delta_s$, defined as the distance between the coverage and the points of maximum velocities. The associated momentum boundary layer thickness can be estimated accordingly and is summarized in table 1.

The mean velocity profiles are also non-dimensionalized using $u_\tau^s$ and plotted against the inner-scaled distance $\Delta z^+ = (z_{SWL} - z)u_\tau^s/\nu$ using a semilogarithmic coordinate system, as shown in figure 6. For comparison, results from studies on 2-D k-type roughness in the boundary layer with $p/k = 3.33$ (Keirsbulck *et al.* 2002) and channel flow with $p/k = 8$ (Krogstad *et al.* 2005) were included due to their geometric similarity. In this context, the bar spacing $p$ from the literature corresponds to the length of a module section in the present study, leading to a ratio of $p/k = 50$, with bar widths of $30k$ and $15k$ for 60 % and 30 % coverage, respectively. It is important to note that in the literature, the bar width is typically assumed to be the same as $k$, with variations in longitudinal separation between consecutive bars being the primary focus. As shown in figure 6, the roughness function $\Delta U^+$ for the 60 % and 30 % coverage for the 60 % and 30 % coverage scenarios is only one-quarter of that observed for 2-D k-type roughness. Additionally, the smaller 30 % coverage results in a greater velocity defect compared with the larger coverage.

## 5.2. *Turbulence intensities and Reynolds sheer stress*

The profiles of turbulent intensities are plotted against the outer-scaled distance relative to the roughness in figures 7 and 8. The 60 %, and 30 % coverage scenarios display similarity in the distribution of turbulent intensities with that observed on 2-D k-type roughness, despite the shift of magnitudes. Specifically, in the streamwise direction, the 30 % coverage exhibits an increase of 25 %, while the 60 % coverage shows comparable magnitudes with the 100 % and 0 % coverages as well as other 2-D k-type roughness. A similar pattern can also be observed in the wall-normal direction, except for the boundary layer with $p/k = 3.33$ which shows a slight increase. Additionally, both the streamwise and
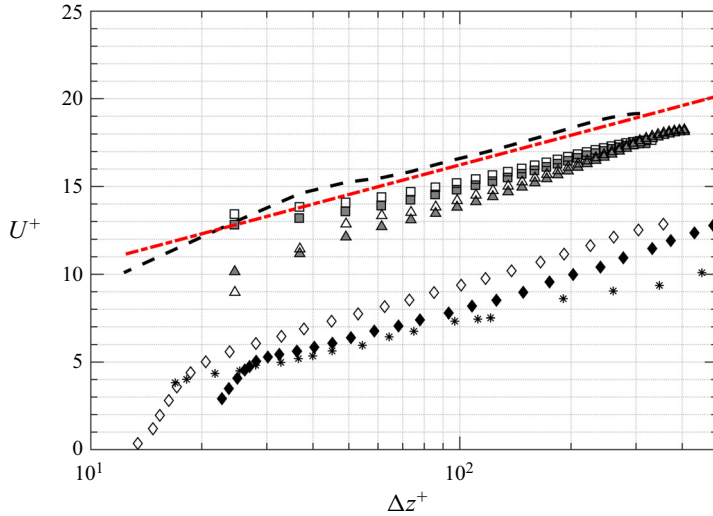
**1000** A6-13

Figure 6. Inner-scaled mean streamwise velocity. Symbols as in figure 5; $*$, boundary layer with $p/k = 3.33$ (Keirsbulck *et al.* 2002), $\blacklozenge$ and $\lozenge$, channel flow with $p/k = 8$ at $Re_\tau = 400$ and 600, respectively (Krogstad *et al.* 2005).
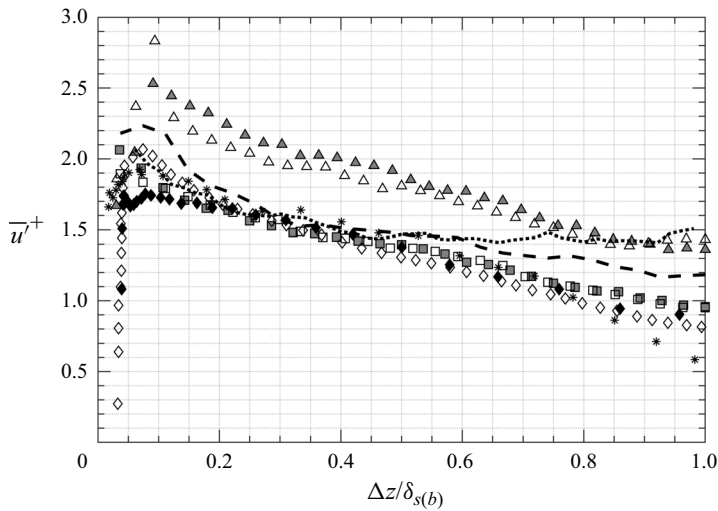


Figure 7. Streamwise velocity fluctuations $\overline{u'}^+ = \sqrt{\overline{u'^2}}/u_\tau^s$ modified by different coverages. Symbols as in figure 5 and 6.

wall-normal turbulence intensities beneath the cover strip are higher than that beneath the air strip.

The profiles of Reynolds sheer stress are plotted against the outer-scaled distance relative to the roughness in figure 9. Similar to the behaviour observed with 2-D k-type roughness, there is an increase in Reynolds shear stress for the 60 % and 30 % coverage compared with 100 % and 0 % coverage. However, the increase for the 30 % coverage, which is up to 60 % compared with 100 % coverage, spans the outer layer and exhibits significant differences between the cover and air strips. These observations for the 30 % coverage indicate different regimes compared with previous studies on 2-D k-type roughness. Specifically,
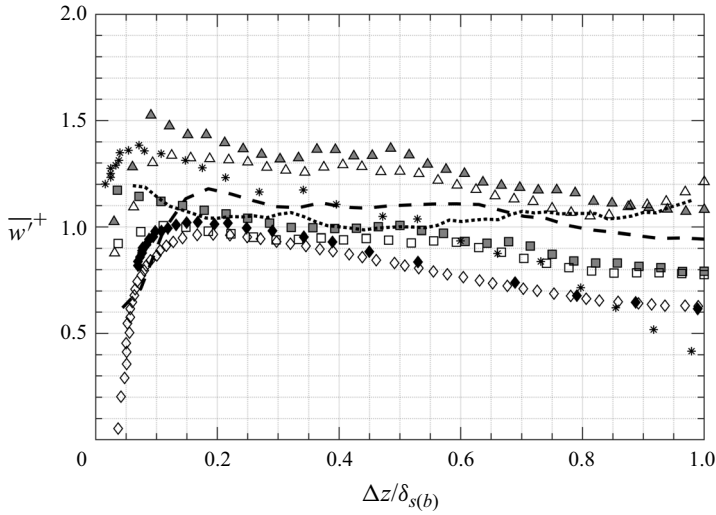
**1000** A6-14

Figure 8. Wall-normal velocity fluctuations $\overline{w'}^+ = \sqrt{\overline{w'^2}}/u_\tau^s$ modified by different coverages. Symbols as in figure 5 and 6.
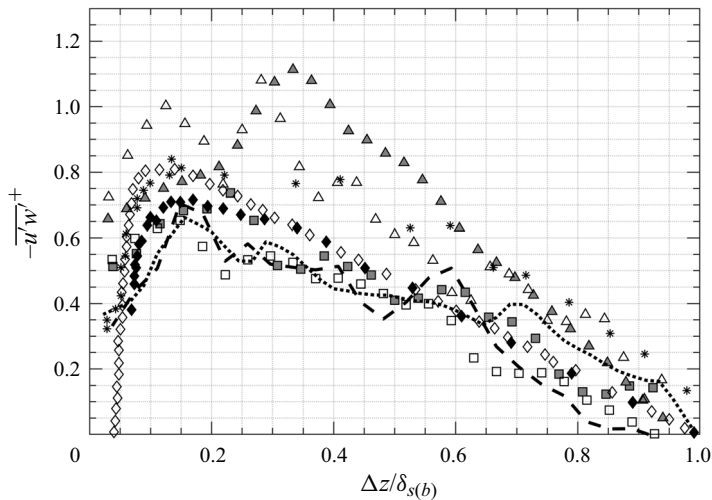


Figure 9. Reynold stress $\overline{u'w'}^+ = \overline{u'w'}/u_\tau^{s\,2}$ modified by different coverages. Symbols as in figures 5 and 6.

for the 60 % coverage, the Reynolds stress beneath the coverage is more positive compared with the 100 % coverage, yet the zero Reynolds stress point remains close to that of the 100 % coverage. This indicates that the periodic coverages induce higher shearing effects, which corresponds to the slight decrease in mean velocity shown in figure 5. Moreover, for the 30 % coverage, the shearing effects due to the periodic coverages are more pronounced, resulting in higher Reynolds stress and a declining shift in the zero Reynolds stress point (larger boundary layer thickness). This also accounts for the greater decrease in the mean velocity profile.

Across different cross-sections, the Reynolds stress beneath the cover strip exhibits an increasing trend from $\Delta z/\delta_s = 0.05$ to 0.3 for the 30 % coverage, while 0.1 for the 30 % coverage. The Reynolds stress values near the cover strip are also lower than those near the
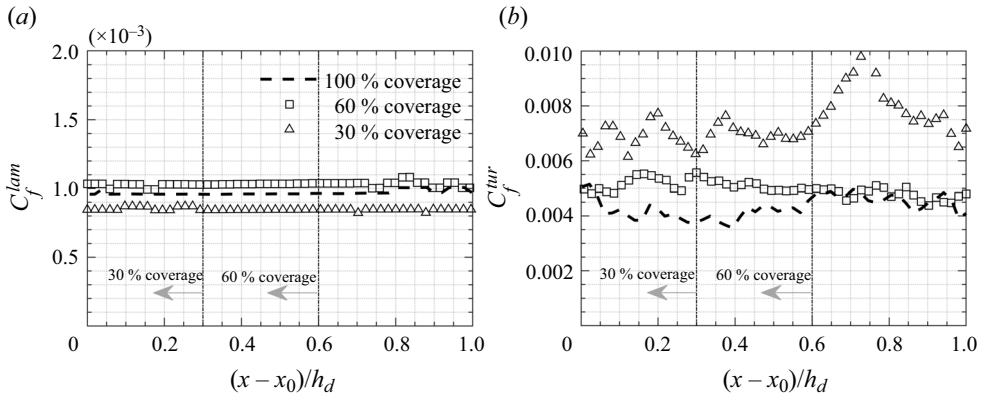
Figure 10. Skin friction contributed by the (*a*) laminar component and the (*b*) turbulent component.

corresponding air strip. While this pattern is also observed in the 60 % coverage scenario, it is less pronounced. This is attributed to the formation of an internal boundary layer (Bou-Zeid *et al.* 2020; Kadivar *et al.* 2021) due to the sudden change of roughness from the air strip to the cover strip, which results in more pronounced shearing effects. Although the internal boundary layer does not become fully developed due to the short length of the cover strip, it accounts for the lower Reynolds stress in its vicinity. Moving into the air strip, the flow is no longer subjected to high shearing, and the momentum exchange in the wall-normal direction smooths the transition.

### 5.3. *Skin friction and wall shear stress*

Figure 10 plots the decomposed contributions to local skin friction along the streamwise distance within one module section, as calculated by (3.2). In figure 10(*a*), the laminar component is shown to remain relatively uniform across the streamwise distance, with the 30 % coverage showing slightly lower values compared with the 60 % and 100 % coverage cases. In contrast, figure 10(*b*) highlights the turbulent component, which is significantly higher than the laminar component. The 100 % coverage maintains a stable and lower turbulent skin friction, while the 60 % coverage shows similar behaviour but with slightly higher values of turbulent skin friction under the coverage strip. Comparatively, the 30 % coverage case exhibits pronounced fluctuations, with a significant increase in turbulent skin friction under the air strip. The fluctuations illustrate the complexity of the flow pattern in the 30 % coverage case. These findings highlight the distinct behaviour between the 60 % and 30 % coverage regimes, which is consistent with the higher turbulent intensity and Reynolds shear stress observed in the 30 % coverage discussed earlier.

Figure 11 plots the non-dimensional shear stress calculated using (3.3) as a function of the normalized wall-normal distance. As expected, the viscous component dominates in the near-wall region and becomes minimal in the outer flow. A decrease in the viscous component can be observed from the air strip to the cover strip due to the internal boundary layer for both the 60 % and 30 % coverage cases. The increase of total shear stress for 60 % coverage in the near-wall region from the cover strip to the air strip is primarily due to the rise in the viscous component, as the turbulent contribution shown in figure 9 remains relatively consistent. In contrast, for the 30 % coverage, the similar increase in total shear stress is attributed to the increase in both the viscous and turbulent components.
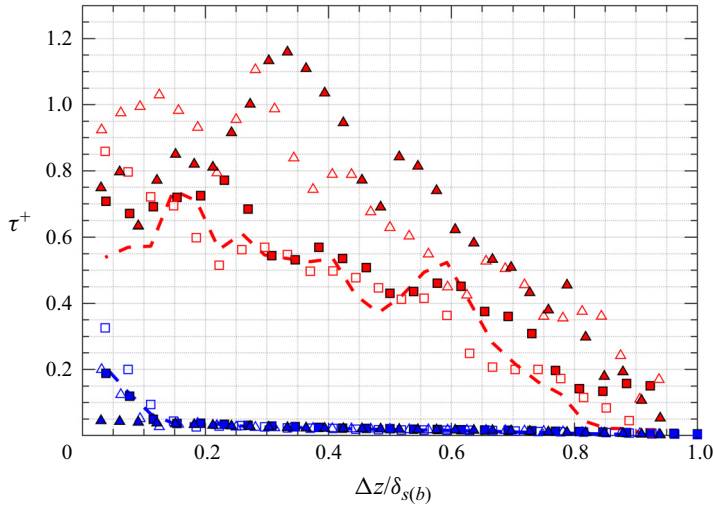
**1000** A6-16

Figure 11. Decomposition of the total shear stress $\tau^+ = \tau/u_\tau^{s\,2}$. Symbols as in figure 5, with the red and blue colours representing the total shear stress and the viscous component, respectively.

## 6. Spanwise vortices

### 6.1. *Instantaneous examples of spanwise vortices*

In the previous section, it can be observed that the 60 % and 30 % coverage scenarios exhibit distinct flow regimes. In the literature, the effects of 2-D k-type roughness are typically confined to the near-wall region (Volino, Schultz & Flack 2009; Kadivar *et al.* 2021), while larger spacing between bars tends to induce higher Reynolds normal stress and shear stress (Lee *et al.* 2011). The flow behaviour beneath the 60 % coverage aligns with this pattern, with the impact on flow properties primarily confined to the near-wall region. In contrast, the 30 % coverage was found to influence the flow differently, resulting in a significant increase in Reynolds normal stress and shear stress across the outer layer. This type of roughness effect has not previously been reported as far as we are aware. However, similarities were also noted between the 60 % and 30 % coverage cases. In both scenarios, turbulent normal stress decreases from the cover strip to the air strip, while total shear stress increases. To further investigate these differences, the turbulent structures are analysed in the subsequent sections.

Instantaneous examples of prograde and retrograde spanwise vortices are examined in this section. Figures 12 and 13 depict an instantaneous velocity realization in the streamwise–wall-normal plane for each coverage scenario, visualized using Galilean decomposition. A constant advection velocity of $U_c \approx 0.6U_{max}$ is subtracted from all streamwise components in figure 12 to emphasize the near-wall region, while $U_c \approx 0.75U_{max}$ is applied in figure 13 to highlight the outer-layer region. Note that there is a minor adjustment on $U_c$ for each case to obtain the best visualization. Contours of instantaneous $\Lambda_{ci}$, calculated using (3.4) and (3.5) described in § 3.1, are overlaid on figures 12 and 13. It is observed that the distribution of $\Lambda_{ci}$ aligns well with the vortex structures visualized via Galilean decomposition, although identifying regions where $\Lambda_{ci}$ spans only a limited number of grid points can be challenging through direct visualization techniques.

For the 100 % coverage scenario shown in figures 12(*a*) and 13(*a*), the prograde structures are seen to induce vigorous ejections of low-speed fluid just above and upstream
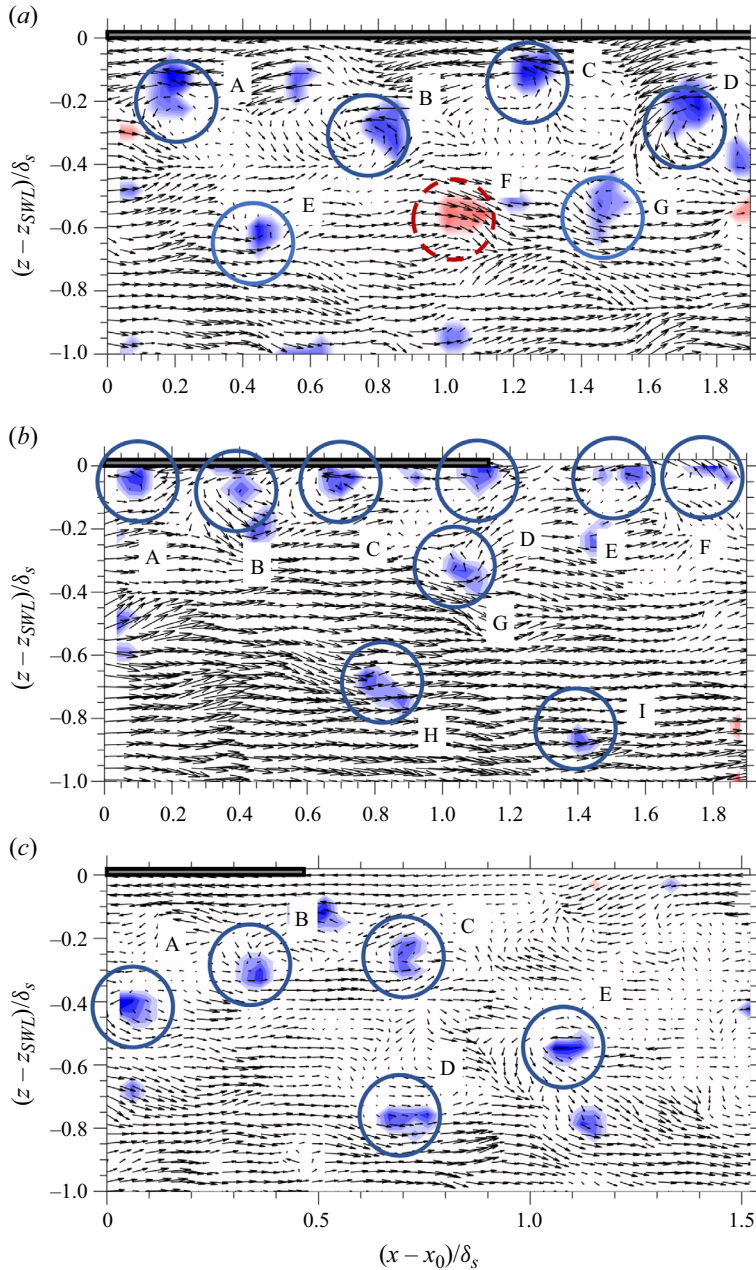
Figure 12. Examples of prograde and retrograde spanwise vortices via Galilean decomposition of instantaneous velocity fields in the streamwise–wall-normal plane of (*a*) 100 % coverage, (*b*) 60 % coverage and (*c*) 30 % coverage. Here $U_c \approx 0.6U_{max}$. The blue colour indicates prograde vortices ($\lambda_{ci} < -1.5$) while the red colour indicates retrograde vortices ($\lambda_{ci} > 1.5$).

of their cores, consistent with the hairpin vortex signature proposed by Adrian *et al.* (2000). The spatial characteristics of the prograde structures align with the hairpin vortex signature and exhibit a slight inclination away from the wall, resembling a hairpin packet
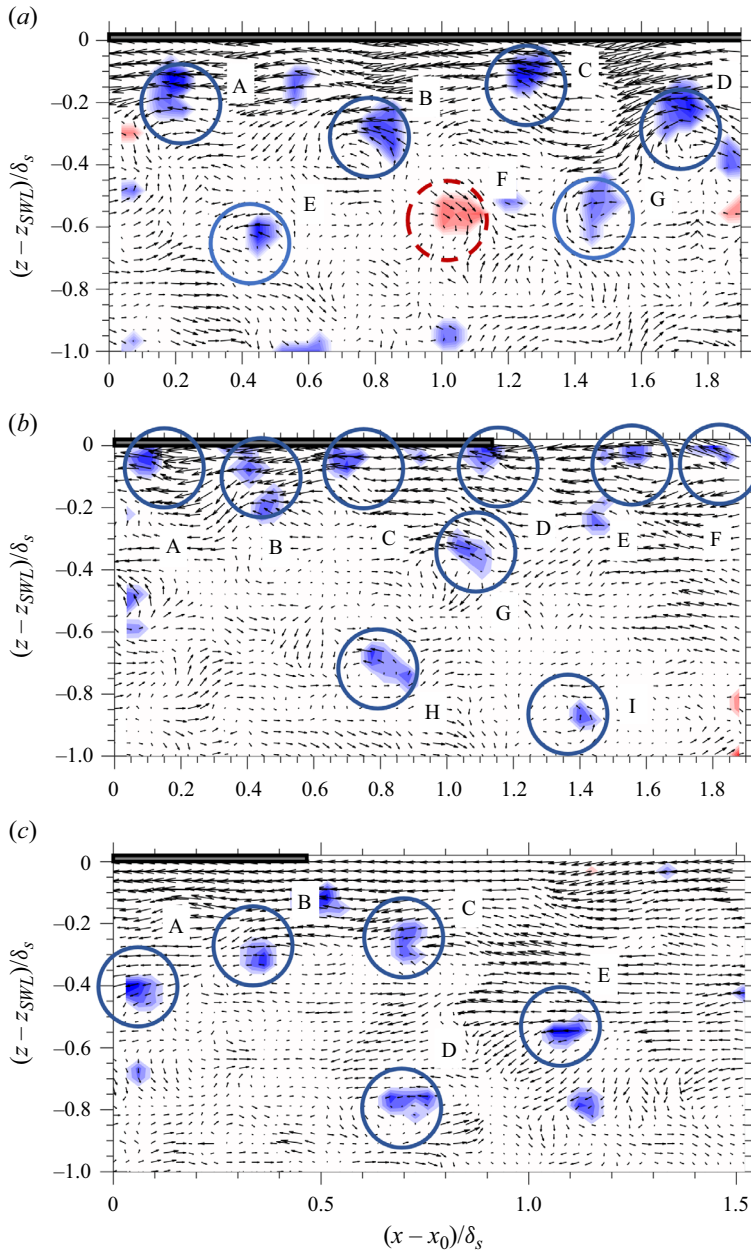
**1000** A6-18

Figure 13. Examples of prograde and retrograde spanwise vortices via Galilean decomposition of instantaneous velocity fields in the streamwise–wall-normal plane of (*a*) 100 % coverage, (*b*) 60 % coverage and (*c*) 30 % coverage. Here $U_c \approx 0.75 U_{max}$. The blue colour indicates prograde vortices ($\lambda_{ci} < -1.5$) while the red colour indicates retrograde vortices ($\lambda_{ci} > 1.5$).

(e.g. vortex pair A, B or pair C, D). A retrograde vortex is also observed in this instance, nesting along the outer edge of the hairpin packet near prograde vortex B.

For the 60 % coverage scenario shown in figures 12(*b*) and 13(*b*), vortex structures in the form of packets are still present, although they tend to cluster in the near-wall region and advect with the flow. The inclining angle of these structures decreases compared with

the 100 % scenario. In contrast, for the 30 % coverage scenario shown in figures 12(*c*) and 13(*c*), vortex structures in the near-wall region primarily cluster near the cover strip region, indicating a general trend where the envelope of vortex structures generated from the cover strip inclines away from the entire coverage.

Adrian *et al.* (2000) proposed that the packets of the harpins exhibited characteristic growth angles determined by their envelope, where newer, smaller packets propagated more slowly than older, larger ones. Dennis & Nickels (2011) observed that averaged hairpin vortices maintained consistent shapes throughout the boundary layer's height, with angle and size variations that scaled proportionally with their height in the boundary layer. These observations suggest that when older, larger packets encounter newer, smaller and slower-moving packets downstream, they experience strong low-speed fluid ejections just below and upstream of the downstream packets, causing them to lean farther away from the wall. This process, characterized by self-similarity, leads to distinctive growth angles. Our observations of spanwise vortices in the 100 % coverage scenario align with these findings. However, the 60 % coverage scenario deviates from these conclusions due to the absence of new packet generation beneath the air strip. This results in packet overstretching upstream and a decreased lean away from the wall. Conversely, these conclusions incompletely explain the 30 % coverage scenario's observations. While the envelopes of spanwise vortices are evident, there is a noticeable increase in smaller-core vortexes, particularly in the air strip region. This suggests the presence of flow detachment downstream of the cover strip, leading to the transformation from large to small vortexes.

Therefore, it is the presence of flow detachment downstream of the periodic cover strips that causes the flow to behave differently in the 30 % coverage scenario compared with conventional 2-D roughness. In previous studies of rough-to-smooth transitions, the internal boundary layer forms slowly, with the intense turbulence from the rough surface dictating the adjustment rate to the smooth surface conditions (Antonia & Luxton 1972; Kadivar *et al.* 2021). The inner layer gradually adapts to the transition, leading to a slower recovery of the boundary layer to a self-preserving state. Comparatively, with the periodic coverage in this study, the internal boundary layer becomes unstable beneath the air strips without the production of turbulence.

### 6.2. *Population trends and characteristics of spanwise vortices*

The population trends of both prograde and retrograde spanwise vortices can be analysed using (3.6) as a function of wall-normal position, which evaluates the spatial location of each vortex from the instantaneous $\Lambda_{ci}$ fields. Figure 14(*a,b*) depict the outer-scaled prograde and retrograde population densities, $\Pi_p$ and $\Pi_r$, respectively, as a function of $\Delta z/\delta_s$. These trends are consistent in magnitude with other boundary flows at comparable Reynolds numbers. Prograde spanwise vortices exhibit their highest population densities near the wall ($\Delta z < 0.2\delta_s$) for all three coverages, with $\Pi_p$ monotonically decreasing with $\Delta z$ across all coverages, akin to other turbulent layers. Comparing the 60 % coverage scenario with the 100 % coverage scenario reveals a lower maximum in the near-wall region for the former, attributed to the lack of harpin vortex generation beneath the air strip. However, both scenarios show comparable trends in the outer layer, indicating similar collection behaviours of vortex packets. In contrast, the 30 % coverage scenario demonstrates a higher magnitude in vortex population, attributed to the generation of smaller but more numerous vortexes due to flow detachment. On the other hand, $\Pi_r$ for the 100 % and 60 % coverage cases steadily increases away from the wall, reaching a local maximum near the outer edge of the log layer. Beyond this layer, influenced by the opposite boundaries, $\Pi_r$ rises again and peaks at $z = \delta_s$, resembling behaviour observed in channel
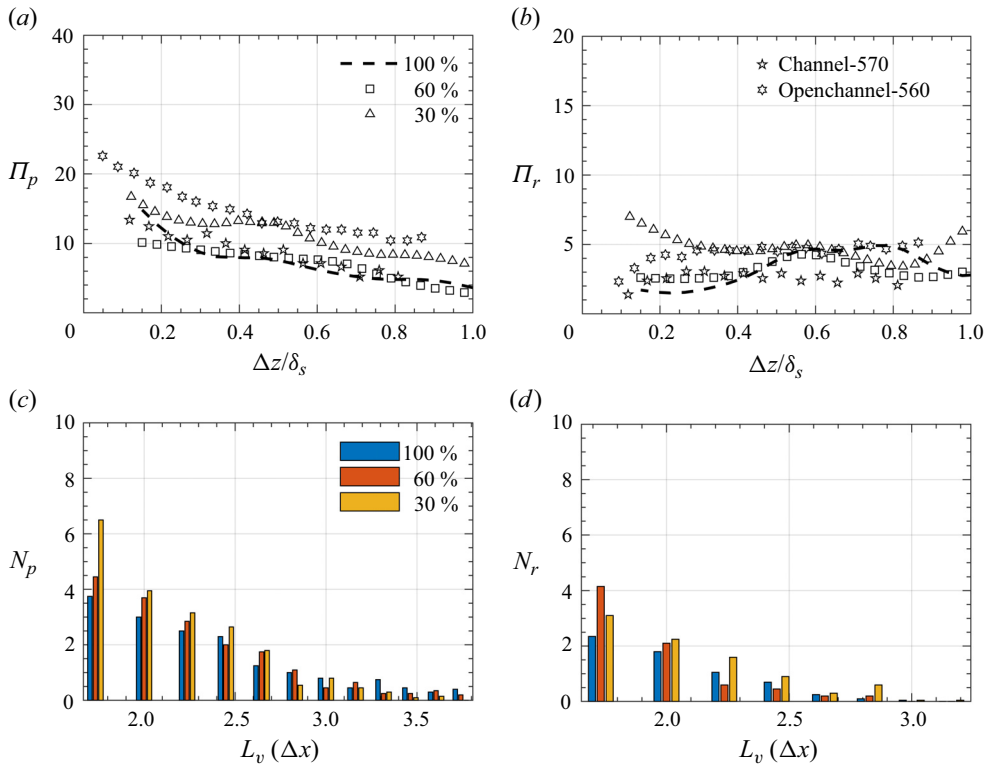
Figure 14. (*a*,*b*) Outer-scaled prograde and retrograde vortex population densities, $\Pi_p$ and $\Pi_r$, calculated by (3.6); (*c*,*d*) statistical distribution of sizes for prograde and retrograde vortexes. The results of channel flow (Channel-570) are from Wu & Christensen (2006) with $Re_\tau = 570$ and the results of open-channel flow (Openchannel-560) are from Zhong *et al.* (2015) with $Re_\tau = 560$.

flow. However, the 30 % coverage scenario diverges from this trend by starting with a maximum, highlighting differences in retrograde vortex generation mechanisms.

Vortex size plays a significant role as an index for characterizing modifications in turbulent structure due to different coverages. Vortex cross-sectional length ($L_v = \sqrt{A_v}$) is used to compute the diameter for each identified vortex section ($A_v$ represents the area the vortex spans). Figure 14(*c*,*d*) display histogram distributions of the average number of prograde and retrograde spanwise vortices, respectively, against cross-sectional length. The unit of cross-sectional length is chosen as the streamwise spatial resolution. As the area size of each vortex section depends on the number of grid cells, a discrete distribution is obtained. The sectional lengths for all coverages cluster within the range of $1.7\Delta x$ to $2.8\Delta x$, with varying percentage decreases from the lowest sectional length. Notably, partial coverage scenarios exhibit a higher percentage of low sectional lengths. The weighted average sectional lengths of prograde and retrograde spanwise vortices for each case are summarized in table 3. Compared with the range of 35–44 for $L_v^{p+}$ reported by Carlier & Stanislas (2005) and 45–52 by Wu & Christensen (2006), the mean value for 100 % coverage in our study is slightly lower. This discrepancy may be due to the resolution limitations or the differences in Reynolds numbers and the Reynolds number dependence of spanwise vortices is observed in the above literature. The average sectional lengths of prograde vortices tend to decrease as the coverage percentage increases. Specifically, there is a reduction of one quarter in the mean sectional lengths of prograde vortices

| Test | $L_v^p \, (\Delta x)$ | $L_v^{p+}$ | $L_v^r \, (\Delta x)$ | $L_v^{r+}$ |
|------|------|------|------|------|
| T1 | 2.5 | 34 | 2.1 | 28 |
| T2 | 2.3 | 31 | 2.0 | 27 |
| T3 | 2.2 | 29 | 2.0 | 27 |

Table 3. Weighted average sectional lengths of spanwise vortices: $L_v^p$, sectional lengths of prograde vortices with $\Delta x$ as units; $L_v^{p+}$, inner-scaled values; $L_v^r$ and $L_v^{r+}$, sectional lengths and inner-scaled values of retrograde vortices, respectively.

from 100 % coverage to 30 % coverage. On the other hand, the mean sectional lengths of retrograde vortices are smaller compared with their corresponding prograde counterparts, but they do not exhibit a diminishing trend with the increase in partial percentage. This observation could be attributed to the exclusion of vortices with lower sectional lengths due to limitations in resolution.

Based on our findings, it is reasonable to infer that the absence of hairpin vortices beneath the air strip region causes the overstretching of packets of hairpins generated by the corresponding cover strip upstream. However, this elongation process has its limits related to the opening percentage; once it has exceeded a certain percentage, the formation of a large collection of the packets spanning a significant portion of the boundary layer near continuous boundaries ceases. Subsequently, flow detachment becomes dominant, leading to the destruction of the packets as large vortices transition into smaller ones. The 100 % coverage scenario aligns well with conventional conclusions. In the 60 % coverage scenario, we observe the overstretching phenomenon but the collection behaviour of hairpin vortices persists, albeit with some flow phenomena evidenced by the decrease in mean sectional lengths of prograde vortices. In the 30 % coverage scenario, flow detachment becomes dominant, resulting in a significant decrease in mean sectional lengths and an increase in the population of prograde vortices. This change also leads to an increase in retrograde vortex population in the near-boundary region. However, a clear relationship between the sizes of prograde and retrograde spanwise vortices remains elusive. In the literature, these retrograde structures may be the by-product of the local dynamics of prograde vortices, as suggested by Yang, Meng & Sheng (2001), or the merging of hairpin structures as proposed by Tomkins & Adrian (2003). Due to resolution limitations, we are unable to delve deeply into the study of the relationship between the sizes of prograde and retrograde spanwise vortices. Nevertheless, streamwise-aligned prograde vortices with signatures consistent with hairpin structures still dominate the majority of boundary layer structure analysis, given the relatively insignificant number of retrograde vortices.

## 7. Premultiplied spectra

Our observations indicate that the increasing dominance of flow detachment with decreasing coverage percentage, resulting in a greater population of smaller spanwise vortices especially for 30 % coverage. However, Heisel *et al.* (2021) mentioned that a cluster of high-intensity $\lambda_{ci}$ may comprise a possible cluster of smaller vortices. To further examine the observations, the premultiplied power spectrum is employed to illustrate the contribution associated with varying wavenumbers across different coverages. To investigate the structural differences resulting from periodic coverages, we compare the premultiplied spectra of turbulence intensity, or equivalently the fraction of TKE, $k_x \Phi_{u'u'}$,
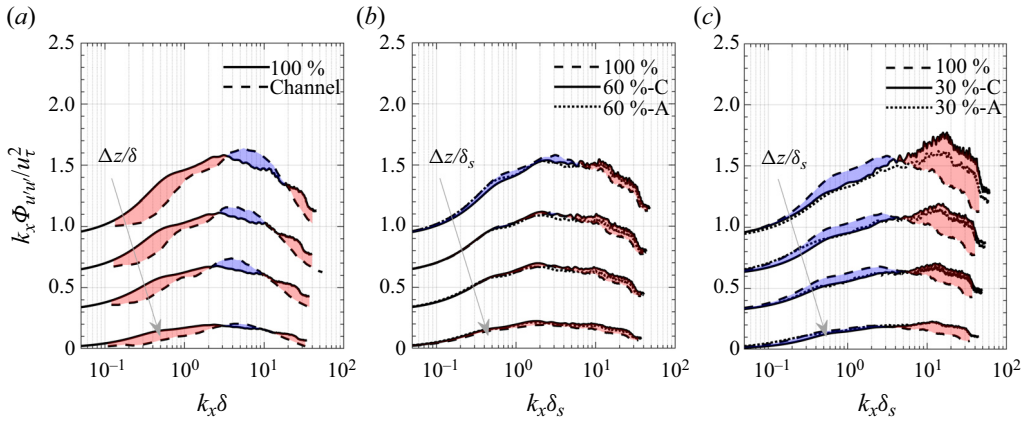
Figure 15. Premultiplied power spectra of streamwise velocity fluctuations at different distances from respective boundaries. (*a*) Boundary layers with the 100 % coverage and over a channel wall; (*b*) boundary layers with the 100 % and 60 % coverage, where 'C' and 'A' represent cross-sections beneath the cover and air strip, respectively; (*c*) boundary layers with the 100 % and 30 % coverage. The data of closed channel flow with $Re_\tau = 531$ are from Balakumar & Adrian (2007). The spectral curves for $\Delta z/\delta = 0.12$, 0.28, 0.46 and 0.77 are presented from top to bottom, each line incremented by 0.3.

at various $z$ positions across different conditions, as depicted in figure 15. It is noted that the spectral curves for $\Delta z/\delta_s = 0.12$, 0.28, 0.46 and 0.77 are presented from top to bottom, each line incremented by 0.3. Initially, in figure 15(*a*), we validate our results by comparing the upper boundary layer beneath the 100 % coverage with canonical channel flow data ($Re_\tau = 531$) from Balakumar & Adrian (2007). Compared with the literature data, the marginal disparity could stem from differences in Reynolds number and experimental configurations. Moreover, higher contributions at high $k_x\delta_s$ may be influenced by measurement noise. Overall, our postprocessed results enable the analysis of energy contributions across different wavenumbers.

In figure 15(*b*), we compare the 60 % coverage scenario, including various cross-sections, with the 100 % coverage scenario. The energy contributions closely align for these cross-sections, with the 60 % coverage scenario generally mirroring the trend observed in 100 % coverage, albeit with slightly higher contributions at high wavenumbers. This correspondence with the spanwise vortex findings suggests a similarity in the contribution from varying wavenumbers, indicative of the collection behaviour of hairpin packets, despite packet overstretching in the near-wall region. Additionally, the higher contributions at high wavenumbers, indicating small-scale motions, correspond to the increased percentage of smaller vortices.

Moving to figure 15(*c*), where we compare the 30 % coverage scenario with 100 % coverage, much higher energy contributions can be observed beneath the cover strip compared with the air strip, especially in the high wavenumber region. The disparity between the two cross-sections diminishes with increasing distance from the coverage. Unlike the shape seen in the 100 % coverage scenario, we can observe a notable decrease in contributions from low wavenumbers and a significant increase in contributions from high wavenumbers. These observations underscore the dominance of small-scale motions, aligning with the marked increase in smaller spanwise vortices and hinting at the presence of flow detachment.

According to Kolmogorov's hypothesis (Kolmogorov 1962), TKE is primarily carried by the low wavenumber range (large-scale motions or vortices) and dissipates in the high

wavenumber range (small-scale motions or vortices). The transition from large-scale to small-scale motions involves a transfer of TKE from low to high wavenumbers. Our study's observations reveal that with decreasing coverage, the contribution from the high wavenumber range increases, indicating more energy transfer from the low wavenumber range and heightened energy dissipation. This contributes to the reduction in bulk velocity and a more pronounced decrease in mean velocity near the coverage.

## 8. The contribution of VLSMs

In the previous sections, it was observed that the 30 % coverage significantly enhances turbulence in the outer layer beneath the cover strip while the 60 % coverage does not exhibit the same effect. This highlights the importance of investigating large scale motions related to the outer layer. The studies across various types of TBLs, including pipe flow, channel flow, planetary boundary layer and open channel flow (Guala *et al.* 2006; Balakumar & Adrian 2007; Duan *et al.* 2020*a*), showed that VLSMs not only carried more than half of the kinetic energy but also more than half of the Reynolds shear stress. Given that our study focuses on relatively small Reynolds numbers, we regarded the range of $k_x \delta_s \geq 2$ as the contribution from VLSMs, corresponding to wavelength of $\pi \delta_s$, by following Balakumar & Adrian (2007). The contributions to kinetic energy or Reynolds stress carried by VLSMs can be defined as

$$\Gamma_{u_i' u_j'} = \frac{\int_0^{2/\delta} \Phi_{u_i' u_j'}(k_x)\, \mathrm{d}k_x}{\int_0^{\infty} \Phi_{u_i' u_j'}(k_x)\, \mathrm{d}k_x}. \tag{8.1}$$

The variation of $\Gamma_{u'u'}$ and $\Gamma_{u'w'}$ as a function of $\Delta z/\delta_s$ is presented in figure 16, wherein results from other wall-bounded flows are also incorporated for comparative analysis. In the outer region of 100 % and 60 % coverage (e.g. $\Delta z/\delta_s > 0.2$), as illustrated in figure 16(*a*), the contribution of VLSMs to kinetic energy is approximately 0.45, which is lower than that observed in channel and open-channel flows but comparable to TBLs. This disparity could stem from the low Reynolds number, as discussed in Balakumar & Adrian (2007), or alterations in flow geometry possibly attributed to boundary displacement. Furthermore, in the inner region of 60 % coverage, $\Gamma_{u'u'}$ is slightly higher than that of the 100 % coverage, while lower in the outer region. Conversely, the contribution of VLSMs to kinetic energy in the 30 % coverage scenario is approximately 0.3, marking a one-third decrease compared with the 100 % and 60 % scenarios. All three cases exhibit a similar increasing trend, rising drastically in the inner layer and marginally in the outer layer, aligning with observations in other types of wall-bounded flows.

In contrast, the contribution of VLSMs to Reynolds stress $\Gamma_{u'w'}$ for all three coverages, as presented in figure 16(*b*), follows similar trends to those observed for kinetic energy. The magnitudes for 100 % and 60 % coverage hover around 0.4, decreasing to 0.35 for 30 % coverage, comparable to TBLs and slightly lower than channel flows. In the case of open-channel flow, the trend line ascends from the inner layer to the middle and then sharply declines near the surface. Closed-channel flows and TBLs exhibit similarities in the inner and log layers but experience slight decreases near the outer region's end. However, all three coverages display a slight increase in this region, attributed to slightly higher values generated by the bottom boundary.

Overall, the portion of kinetic energy and Reynolds stress carried by VLSMs decreased from 40 %–50 % in the 100 % and 60 % coverage scenarios to 30 %–40 % in the 30 % coverage scenario. This suggests that the formation of VLSMs is inhibited in the 30 % coverage case. The formation and evolution of VLSMs, however, remain elusive, although
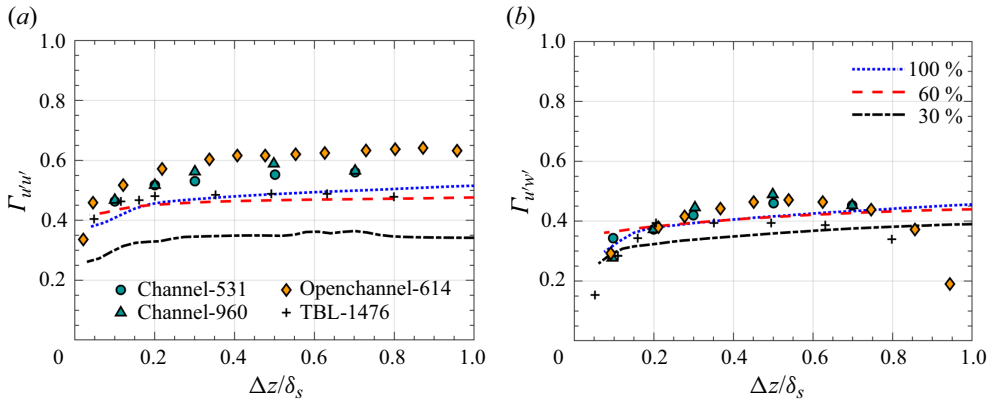
Figure 16. The fraction of (*a*) kinetic energy and (*b*) Reynolds stress carried by VLSMs, $\Gamma_{u'u'}$ and $\Gamma_{u'w'}$.

their interaction with near-wall structures, such as hairpin packets, has been established. Zhou *et al.* (1999) proposed that hairpins initiate bulges, growing both vertically and streamwise until they attain a certain height, thus forming the VLSMs (referred as autogeneration mechanisms). Additionally, hairpin packets are considered the source of long streamwise initial disturbances, which are amplified by flow instability to form long outer modes (referred as amplification mechanisms). Del Alamo & Jimenez (2006) predicted structures as long as $40\delta$, and evidence for outer modes organizing wall vortices can be found in the DNS simulations of Toh & Itano (2005) and Iwamoto, Kasagi & Suzuki (2005). Deshpande, de Silva & Marusic (2023) experimentally observed streamwise-elongated motions extending up to 12 times boundary layer thickness, and the superstructures appeared as an assemblage of the attached eddy hierarchy in the streamwise wall-normal plane suggesting a well-defined spatial organization of the attached eddies. In our study, the 60 % coverage yields kinetic energy contributions from various wavenumbers similar to those of the 100 % coverage, suggesting the generation of comparable VLSMs despite the slight decrease in the inclining angle of the hairpin packets due to their reduced generation. This implies that if the autogeneration mechanism is valid, the absence of hairpin generation would diminish VLSMs, which is contrary to our observations. Moreover, if the amplification mechanism holds true, hairpin packets in the 60 % coverage scenario may persist and evolve into longer outer modes. However, comparing the 60 % and 30 % coverage reveals that while some kinetic energy is still carried by VLSMs in the 30 % coverage scenario, a significant portion is dissipated, transferring energy from low to high wavenumbers. This raises the question: What is the smallest characteristic length for hairpin packets as an seed mode that can be sustained and amplified? Our findings suggest, in a preliminary manner, that the percentage of coverage plays an important role in the modulation of surface turbulence under the installation which can also potentially affect the air–water exchange in the periodic air strips in the cover. Further research is needed to confirm this aspect comprehensively.

## 9. Conclusions

The present study offers a comprehensive laboratory investigation into the turbulence statistics and structure in fully developed open channel flows with periodic open surface coverages, which can occur with installation of large-scale floating solar farms. The PIV

measurements were conducted to assess the turbulence characteristics beneath varying coverage percentages of 100 %, 60 %, 30 % and 0 %. Key findings are outlined as follows.

(i) The mean velocity profile and other turbulence statistics for the 100 % and 60 % coverage are similar. However, with the 30 % coverage, both the turbulence intensity and Reynolds stress exhibit a substantial increase, reaching up to 50 % higher, and the boundary layer thickness increases by more than 25 %. Additionally, the presence of periodic air strips in both the 60 % and 30 % coverage scenarios slightly enhances the viscous component of the shear stress, with the 30 % coverage scenario promoting the local skin friction by 50 %. These results suggest that turbulence can be promoted at a lower coverage percentage. This finding has an important implication for the design of floating solar farms since the increased surface turbulence can promote the exchange of dissolved oxygen at the air–water interface to compensate for the reduction in contact area due to the cover strips.

(ii) Examination of vortex populations and their spatial features reveals that the periodic openings lead to the elongation of hairpin vortex packets and a reduction in their inclination angle, suggesting a probable limit to the size of coherent structures that can be sustained. Exceeding this threshold leads to flow detachment at the edge of cover strips, which results in the dominance of smaller-scale vortices. This mechanism also explains the higher contribution of turbulence to the local skin friction coefficient beneath the air strip in the 30 % coverage scenario. Furthermore, premultiplied power spectra analysis exhibits a shift in energy transfer towards higher wavenumbers with decreasing percentage of coverage. This shift indicates augmented energy dissipation and a concomitant decrease in the mean flow velocity, confirming the existence of the dominance of smaller-scale vortices due to flow detachment.

(iii) The kinetic energy and Reynolds stress carried by VLSMs amount to approximately 40 %–50 % in the 60 % coverage scenario, while this fraction remains around 30 %–40 % in the 30 % coverage scenario. This reduction suggests that the formation of VLSMs is inhibited in the 30 % coverage case. This finding highlights the need for further research to determine the smallest characteristic length for hairpin vortex packets that can serve as a seed for VLSMs, with implications for understanding the generation mechanisms of these large-scale structures under this type of periodic boundary.

**Declaration of interests.** The authors report no conflict of interest.

**Data availability statement.** The data that support the findings of this study are available from the corresponding author upon reasonable request.

**Author ORCIDs.**

Ⓘ Xiaodong Liu https://orcid.org/0000-0002-3833-1863;

Ⓘ Adrian Wing-Keung Law https://orcid.org/0000-0002-2593-6361.

**1000** A6-26

REFERENCES

ADRIAN, R.J. & MARUSIC, I. 2012 Coherent structures in flow over hydraulic engineering surfaces. *J. Hydraul. Res.* **50** (5), 451–464.

ADRIAN, R.J., MEINHART, C.D. & TOMKINS, C.D. 2000 Vortex organization in the outer region of the turbulent boundary layer. *J. Fluid Mech.* **422**, 1–54.

ADRIAN, R.J. & WESTERWEEL, J. 2011 *Particle Image Velocimetry*. Cambridge University Press.

ANTONIA, R.A. & LUXTON, R.E. 1972 The response of a turbulent boundary layer to a step change in surface roughness. Part 2. Rough-to-smooth. *J. Fluid Mech.* **53** (4), 737–757.

ANTONIA, R.A., TEITEL, M., KIM, J. & BROWNE, L.W.B. 1992 Low-Reynolds-number effects in a fully developed turbulent channel flow. *J. Fluid Mech.* **236**, 579–605.

AZMI, M.S.M., OTHMAN, M.Y.H., RUSLAN, M.H.H., SOPIAN, K. & MAJID, Z.A.A. 2013 Study on electrical power output of floating photovoltaic and conventional photovoltaic. In *AIP Conference Proceedings*, vol. 1571, pp. 95–101. American Institute of Physics.

BALAKUMAR, B.J. & ADRIAN, R.J. 2007 Large-and very-large-scale motions in channel and boundary-layer flows. *Phil. Trans. R. Soc.* A **365** (1852), 665–681.

BI, C. & LAW, A.W.-K. 2023 Co-locating offshore wind and floating solar farms–effect of high wind and wave conditions on solar power performance. *Energy* **266**, 126437.

BON, T. & MEYERS, J. 2022 Stable channel flow with spanwise heterogeneous surface temperature. *J. Fluid Mech.* **933**, A57.

BOU-ZEID, E., ANDERSON, W., KATUL, G.G. & MAHRT, L. 2020 The persistent challenge of surface heterogeneity in boundary-layer meteorology: a review. *Boundary-Layer Meteorol.* **177**, 227–245.

CARDOSO, A.H., GRAF, W.H. & GUST, G. 1989 Uniform flow in a smooth open channel. *J. Hydraul. Res.* **27** (5), 603–616.

CARLIER, J. & STANISLAS, M. 2005 Experimental study of eddy structures in a turbulent boundary layer using particle image velocimetry. *J. Fluid Mech.* **535**, 143–188.

CASTRO, I.P. 2007 Rough-wall boundary layers: mean flow universality. *J. Fluid Mech.* **585**, 469–485.

CHAKRABORTY, P., BALACHANDAR, S. & ADRIAN, R.J. 2005 On the relationships between local vortex identification schemes. *J. Fluid Mech.* **535**, 189–214.

COLES, D. 1956 The law of the wake in the turbulent boundary layer. *J. Fluid Mech.* **1** (2), 191–226.

DAI, J., ZHANG, C., LIM, H.V., ANG, K.K., QIAN, X., WONG, J.L.H., TAN, S.T. & WANG, C.L. 2020 Design and construction of floating modular photovoltaic system for water reservoirs. *Energy* **191**, 116549.

DEL ALAMO, J.C. & JIMENEZ, J. 2006 Linear energy amplification in turbulent channels. *J. Fluid Mech.* **559**, 205–213.

DENNIS, D.J.C. & NICKELS, T.B. 2011 Experimental measurement of large-scale three-dimensional structures in a turbulent boundary layer. Part 1. Vortex packets. *J. Fluid Mech.* **673**, 180–217.

DESHPANDE, R., DE SILVA, C.M. & MARUSIC, I. 2023 Evidence that superstructures comprise self-similar coherent motions in high Reynolds number boundary layers. *J. Fluid Mech.* **969**, A10.

DJENIDI, L., ANTONIA, R.A., AMIELH, M. & ANSELMET, F. 2008 A turbulent boundary layer over a two-dimensional rough wall. *Exp. Fluids* **44**, 37–47.

DUAN, Y., CHEN, Q., LI, D. & ZHONG, Q. 2020*a* Contributions of very large-scale motions to turbulence statistics in open channel flows. *J. Fluid Mech.* **892**, A3.

DUAN, Y., ZHANG, P., ZHONG, Q., ZHU, D. & LI, D. 2020*b* Characteristics of wall-attached motions in open channel flows. *Phys. Fluids* **32** (5), 055110.

FUKAGATA, K., IWAMOTO, K. & KASAGI, N. 2002 Contribution of Reynolds stress distribution to the skin friction in wall-bounded flows. *Phys. Fluids* **14** (11), L73–L76.

GAD-EL HAK, M. & BANDYOPADHYAY, P.R. 1994 Reynolds number effects in wall-bounded turbulent flows. *Appl. Mech. Rev.* **47** (8), 307–365.

GHOSH, A. 2023 A comprehensive review of water based PV: flotavoltaics, under water, offshore & canal top. *Ocean Engng* **281**, 115044.

GUALA, M., HOMMEMA, S.E. & ADRIAN, R.J. 2006 Large-scale and very-large-scale motions in turbulent pipe flow. *J. Fluid Mech.* **554**, 521–542.

HEAD, M.R. & BANDYOPADHYAY, P. 1981 New aspects of turbulent boundary-layer structure. *J. Fluid Mech.* **107**, 297–338.

HEISEL, M., DE SILVA, C.M., HUTCHINS, N., MARUSIC, I. & GUALA, M. 2021 Prograde vortices, internal shear layers and the Taylor microscale in high-Reynolds-number turbulent boundary layers. *J. Fluid Mech.* **920**, A52.

HOYAS, S. & JIMÉNEZ, J. 2008 Reynolds number effects on the Reynolds-stress budgets in turbulent channels. *Phys. Fluids* **20** (10), 101511.

HUANG, G., TANG, Y., CHEN, X., CHEN, M. & JIANG, Y. 2023 A comprehensive review of floating solar plants and potentials for offshore applications. *J. Mar. Sci. Engng* **11** (11), 2064.

IWAMOTO, K., KASAGI, N. & SUZUKI, Y. 2005 Direct numerical simulation of turbulent channel flow at $Re\tau = 2320$. In *Proc. 6th Symp. Smart Control of Turbulence*, pp. 327–333.

KADIVAR, M., TORMEY, D. & McGRANAGHAN, G. 2021 A review on turbulent flow over rough surfaces: fundamentals and theories. *Intl J. Thermofluids* **10**, 100077.

DE KAT, R., GAN, L., DAWSON, J.R. & GANAPATHISUBRAMANI, B. 2013 Limitations of estimating turbulent convection velocities from PIV. arXiv:1311.6400.

KEIRSBULCK, L., LABRAGA, L., MAZOUZ, A. & TOURNIER, C. 2002 Surface roughness effects on turbulent boundary layer structures. *Trans. ASME J. Fluids Engng* **124** (1), 127–135.

KIM, J., MOIN, P. & MOSER, R. 1987 Turbulence statistics in fully developed channel flow at low Reynolds number. *J. Fluid Mech.* **177**, 133–166.

KIM, K.C. & ADRIAN, R.J. 1999 Very large-scale motion in the outer layer. *Phys. Fluids* **11** (2), 417–422.

KIRKGÖZ, M.S. & ARDIÇLIOĞLU, M. 1997 Velocity profiles of developing and developed open channel flow. *ASCE J. Hydraul. Engng* **123** (12), 1099–1105.

KLEBANOFF, P.S. 1955 Characteristics of turbulence in boundary layer with zero pressure gradient. *NASA Tech. Rep.* NACA-TR-1247.

KLINE, S.J., REYNOLDS, W.C., SCHRAUB, F.A. & RUNSTADLER, P.W. 1967 The structure of turbulent boundary layers. *J. Fluid Mech.* **30** (4), 741–773.

KOLMOGOROV, A.N. 1962 A refinement of previous hypotheses concerning the local structure of turbulence in a viscous incompressible fluid at high Reynolds number. *J. Fluid Mech.* **13** (1), 82–85.

KOVASZNAY, L.S.G., KIBENS, V. & BLACKWELDER, R.F. 1970 Large-scale motion in the intermittent region of a turbulent boundary layer. *J. Fluid Mech.* **41** (2), 283–325.

KROGSTAD, P.-Å., ANDERSSON, H.I., BAKKEN, O.M. & ASHRAFIAN, A. 2005 An experimental and numerical study of channel flow with rough walls. *J. Fluid Mech.* **530**, 327–352.

KROGSTADT, P.-Å. & ANTONIA, R.A. 1999 Surface roughness effects in turbulent boundary layers. *Exp. Fluids* **27** (5), 450–460.

LEE, J.H., SUNG, H.J. & KROGSTAD, P.-Å. 2011 Direct numerical simulation of the turbulent boundary layer over a cube-roughened wall. *J. Fluid Mech.* **669**, 397–431.

LIEN, K., MONTY, J.P., CHONG, M.S. & OOI, A. 2004 The entrance length for fully developed turbulent channel flow. In *15th Australian Fluid Mechanics Conference*, vol. 15, pp. 356–363. University of Sydney.

MARUSIC, I. & MONTY, J.P. 2019 Attached eddy model of wall turbulence. *Annu. Rev. Fluid Mech.* **51**, 49–74.

MARUŠIĆ, I. & PERRY, A.E. 1995 A wall-wake model for the turbulence structure of boundary layers. Part 2. Further experimental support. *J. Fluid Mech.* **298**, 389–407.

MARUSIC, I., UDDIN, A.K.M. & PERRY, A.E. 1997 Similarity law for the streamwise turbulence intensity in zero-pressure-gradient turbulent boundary layers. *Phys. Fluids* **9** (12), 3718–3726.

MILLIKAN, C.B. 1938 A critical discussion of turbulent flows in channels and circular tubes. In *Proc. Fifth Intern. Congr. Appl. Mech., Cambridge*, pp. 386–392.

MONTY, J.P., HUTCHINS, N., NG, H.C.H., MARUSIC, I. & CHONG, M.S. 2009 A comparison of turbulent pipe, channel and boundary layer flows. *J. Fluid Mech.* **632**, 431–442.

MOSER, R.D., KIM, J. & MANSOUR, N.N. 1999 Direct numerical simulation of turbulent channel flow up to $Re\tau = 590$. *Phys. Fluids* **11** (4), 943–945.

MUSTE, M., BRAILEANU, F. & ETTEMA, R. 2000 Flow and sediment transport measurements in a simulated ice-covered channel. *Water Resour. Res.* **36** (9), 2711–2720.

NEZU, I. & RODI, W. 1986 Open-channel flow measurements with a laser doppler anemometer. *ASCE J. Hydraul. Engng* **112** (5), 335–355.

POPE, S.B. 2001 Turbulent flows. *Meas. Sci. Technol.* **12** (11), 2020–2021.

ROBERT, A. & TRAN, T. 2012 Mean and turbulent flow fields in a simulated ice-covered channel with a gravel bed: some laboratory observations. *Earth Surf. Process. Landf.* **37** (9), 951–956.

ROBINSON, S.K. 1991 Coherent motions in the turbulent boundary layer. *Annu. Rev. Fluid Mech.* **23** (1), 601–639.

SALESKY, S.T., CALAF, M. & ANDERSON, W. 2022 Unstable turbulent channel flow response to spanwise-heterogeneous heat fluxes: Prandtl's secondary flow of the third kind. *J. Fluid Mech.* **934**, A46.

SHI, W., YAN, C., REN, Z., YUAN, Z., LIU, Y., ZHENG, S., LI, X. & HAN, X. 2023 Review on the development of marine floating photovoltaic systems. *Ocean Engng* **286**, 115560.

SMITH, C.R. & METZLER, S.P. 1983 The characteristics of low-speed streaks in the near-wall region of a turbulent boundary layer. *J. Fluid Mech.* **129**, 27–54.

SPALART, P.R. 1988 Direct simulation of a turbulent boundary layer up to $R\theta = 1410$. *J. Fluid Mech.* **187**, 61–98.

SREE, D.K.K., LAW, A.W.-K., PANG, D.S.C., TAN, S.T., WANG, C.L., KEW, J.H., SEOW, W.K. & LIM, V.H. 2022 Fluid-structural analysis of modular floating solar farms under wave motion. *Solar Energy* **233**, 161–181.

STEFFLER, P.M., RAJARATNAM, N. & PETERSON, A.W. 1985 LDA measurements in open channel. *ASCE J. Hydraul. Engng* **111** (1), 119–130.

STOLL, R. & PORTÉ-AGEL, F. 2009 Surface heterogeneity effects on regional-scale fluxes in stable boundary layers: surface temperature transitions. *J. Atmos. Sci.* **66** (2), 412–431.

STROH, A., SCHÄFER, K., FOROOGHI, P. & FROHNAPFEL, B. 2020 Secondary flow and heat transfer in turbulent flow over streamwise ridges. *Intl J. Heat Fluid Flow* **81**, 108518.

TAYLOR, G.I. 1938 The spectrum of turbulence. *Proc. R. Soc. Lond.* A **164** (919), 476–490.

THIELICKE, W. & SONNTAG, R. 2021 Particle image velocimetry for MATLAB: accuracy and enhanced algorithms in PIVlab. *J. Open Res. Softw.* **9** (1).

TOH, S. & ITANO, T. 2005 Interaction between a large-scale structure and near-wall structures in channel flow. *J. Fluid Mech.* **524**, 249–262.

TOMKINS, C.D. & ADRIAN, R.J. 2003 Spanwise structure and scale growth in turbulent boundary layers. *J. Fluid Mech.* **490**, 37–74.

VAN DRIEST, E.R. 1956 On turbulent flow near a wall. *J. Aeronaut. Sci.* **23** (11), 1007–1011.

VOLINO, R.J., SCHULTZ, M.P. & FLACK, K.A. 2009 Turbulence structure in a boundary layer with two-dimensional roughness. *J. Fluid Mech.* **635**, 75–101.

WANG, F., HUAI, W., GUO, Y. & LIU, M. 2021 Turbulence structure and momentum exchange in compound channel flows with shore ice covered on the floodplains. *Water Resour. Res.* **57** (4), e2020WR028621.

WANG, F., HUAI, W., LIU, M. & FU, X. 2020 Modeling depth-averaged streamwise velocity in straight trapezoidal compound channels with ice cover. *J. Hydrol.* **585**, 124336.

WEI, T. & WILLMARTH, W.W. 1989 Reynolds-number effects on the structure of a turbulent channel flow. *J. Fluid Mech.* **204**, 57–95.

WU, Y. & CHRISTENSEN, K.T. 2006 Population trends of spanwise vortices in wall turbulence. *J. Fluid Mech.* **568**, 55–76.

YANG, W., MENG, H. & SHENG, J. 2001 Dynamics of hairpin vortices generated by a mixing tab in a channel flow. *Exp. Fluids* **30** (6), 705–722.

ZHANG, J., WANG, W., LI, Z., LI, Q., ZHONG, Y., XIA, Z. & QIU, H. 2021 Analytical models of velocity, Reynolds stress and turbulence intensity in ice-covered channels. *Water* **13** (8), 1107.

ZHONG, Q., LI, D., CHEN, Q. & WANG, X. 2015 Coherent structures and their interactions in smooth open channel flows. *Environ. Fluid Mech.* **15**, 653–672.

ZHOU, J., ADRIAN, R.J., BALACHANDAR, S. & KENDALL, T.M. 1999 Mechanisms for generating coherent packets of hairpin vortices in channel flow. *J. Fluid Mech.* **387**, 353–396.